The Company of Biologists

RESEARCH ARTICLE

Neuronal differentiation influences progenitor arrangement in the vertebrate neuroepithelium

Pilar Guerrero[1,*], Ruben Perez-Carrasco[1], Marcin Zagorski[2,‡], David Page[3], Anna Kicheva[2,§], James Briscoe[4,§] and Karen M. Page[1,§]

ABSTRACT

Cell division, movement and differentiation contribute to pattern formation in developing tissues. This is the case in the vertebrate neural tube, in which neurons differentiate in a characteristic pattern from a highly dynamic proliferating pseudostratified epithelium. To investigate how progenitor proliferation and differentiation affect cell arrangement and growth of the neural tube, we used experimental measurements to develop a mechanical model of the apical surface of the neuroepithelium that incorporates the effect of interkinetic nuclear movement and spatially varying rates of neuronal differentiation. Simulations predict that tissue growth and the shape of lineage-related clones of cells differ with the rate of differentiation. Growth is isotropic in regions of high differentiation, but dorsoventrally biased in regions of low differentiation. This is consistent with experimental observations. The absence of directional signalling in the simulations indicates that global mechanical constraints are sufficient to explain the observed differences in anisotropy. This provides insight into how the tissue growth rate affects cell dynamics and growth anisotropy and opens up possibilities to study the coupling between mechanics, pattern formation and growth in the neural tube.

KEY WORDS: Vertex model, Neural tube, Computational modelling, Tissue mechanics, Epithelial mechanics

INTRODUCTION

The mechanisms that control the arrangement of cells in developing tissues involve both molecular and mechanical processes that spatially and temporally coordinate the division, shape, displacement and differentiation of cells. A central challenge is to understand the interplay between tissue growth, pattern formation and the mechanical forces that act to shape tissues during development.

Studies of several systems have begun to provide insight into how these processes are coordinated (Alt et al., 2017; Merkel and

[1]Department of Mathematics, University College London, Gower Street, London WC1E 6BT, UK. [2]IST Austria, Am Campus 1, A - 3400 Klosterneuburg, Austria. [3]Myrtle Software, Second Floor, 50 St. Andrew's Street, Cambridge CB2 3AH, UK. [4]The Francis Crick Institute, 1 Midland Road, London NW1 1AT, UK.
*Present address: Grupo Interdisciplinar de Sistemas Complejos, Departamento de Matemáticas, Universidad Carlos III de Madrid, 28911 Leganes, Madrid, Spain. ‡Present address: Marian Smoluchowski Institute of Physics, Jagiellonian University, Lojasiewicza 11, 30-348 Krakow, Poland.

§Authors for correspondence (anna.kicheva@ist.ac.at; james.briscoe@crick.ac.uk; karen.page@ucl.ac.uk)

A.K., 0000-0003-4509-4998; J.B., 0000-0002-1020-5240; K.M.P., 0000-0003-4189-4664

Manning, 2017). For example, in the *Drosophila* wing imaginal disc a combination of experimental observations, quantitative image analysis and computational modelling have revealed the global patterns of mechanical tension that affect the final size and shape of the wing. These patterns result from spatial differences in proliferation, cell shape, division orientation and exchange of neighbouring cells (Shraiman, 2005; Aegerter-Wilmsen et al., 2010; Aigouy et al., 2010; LeGoff et al., 2013; Mao et al., 2013; Guirao et al., 2015; Kursawe et al., 2015; Dye et al., 2017), as well as external mechanical constraints, such as the attachment of the wing blade to the contracting wing hinge (Aigouy et al., 2010; Sugimura and Ishihara, 2013; Etournay et al., 2015; Ray et al., 2015). Molecularly, wing morphogenesis is influenced by planar-polarity signalling, which influences the apical geometry of cells and the orientation of cell division (Aigouy et al., 2010; Mao et al., 2011).

Similar to imaginal discs, the vertebrate neural tube is a pseudostratified epithelium. During neurulation the neuroepithelium folds at the ventral midline and closes dorsally to form a cylindrical neural tube, with the apical surfaces of neural progenitors facing the interior lumen (Gilbert, 2014). The proliferation of neural progenitors contributes to growth of the neural tube along the anterioposterior (AP) and dorsoventral (DV) axes. In addition, proliferating cells undergo interkinetic nuclear movement (IKNM), during which the nucleus of each cell translocates along the apicobasal axis in synchrony with cell cycle progression (Sauer, 1935). A direct consequence of IKNM is that the apicobasal shape, the apical surface of cells and the interactions between neighbouring cells change in a highly dynamic manner (reviewed by Strzyz et al., 2016).

At the same time as the neural tube grows, long-range signals control patterning by regulating the expression of transcription factors within the tissue (reviewed by Sagner et al., 2018). The dynamics of this regulatory network results in the specification of molecularly distinct domains of progenitor subtypes arranged along the DV axis. Each progenitor domain gives rise to a distinct subtype of postmitotic neurons. As neurons are formed, they delaminate basally from the epithelium to the forming mantle zone. The delamination of newly born neurons contributes to the morphodynamics of the neuroepithelium, further reshaping the arrangement of cells within the neural tube.

Previous studies of the neural tube have indicated that patterning and growth are tightly coordinated. Cell death is negligible and the rate of progenitor proliferation is spatially uniform throughout the epithelium (Kicheva et al., 2014). However, the rates of terminal neuronal differentiation vary depending on progenitor identity. Most notably, starting at mouse embryonic day (E)9.5, motor neuron progenitors (pMN) differentiate at a significantly faster rate than other progenitor subtypes (Ericson et al., 1996; Kicheva et al., 2014). This difference in the rates of terminal differentiation correlated with a difference in clone shape in lineage tracing experiments (Kicheva et al., 2014; Fig. 1A). In particular, although the AP spread of clones
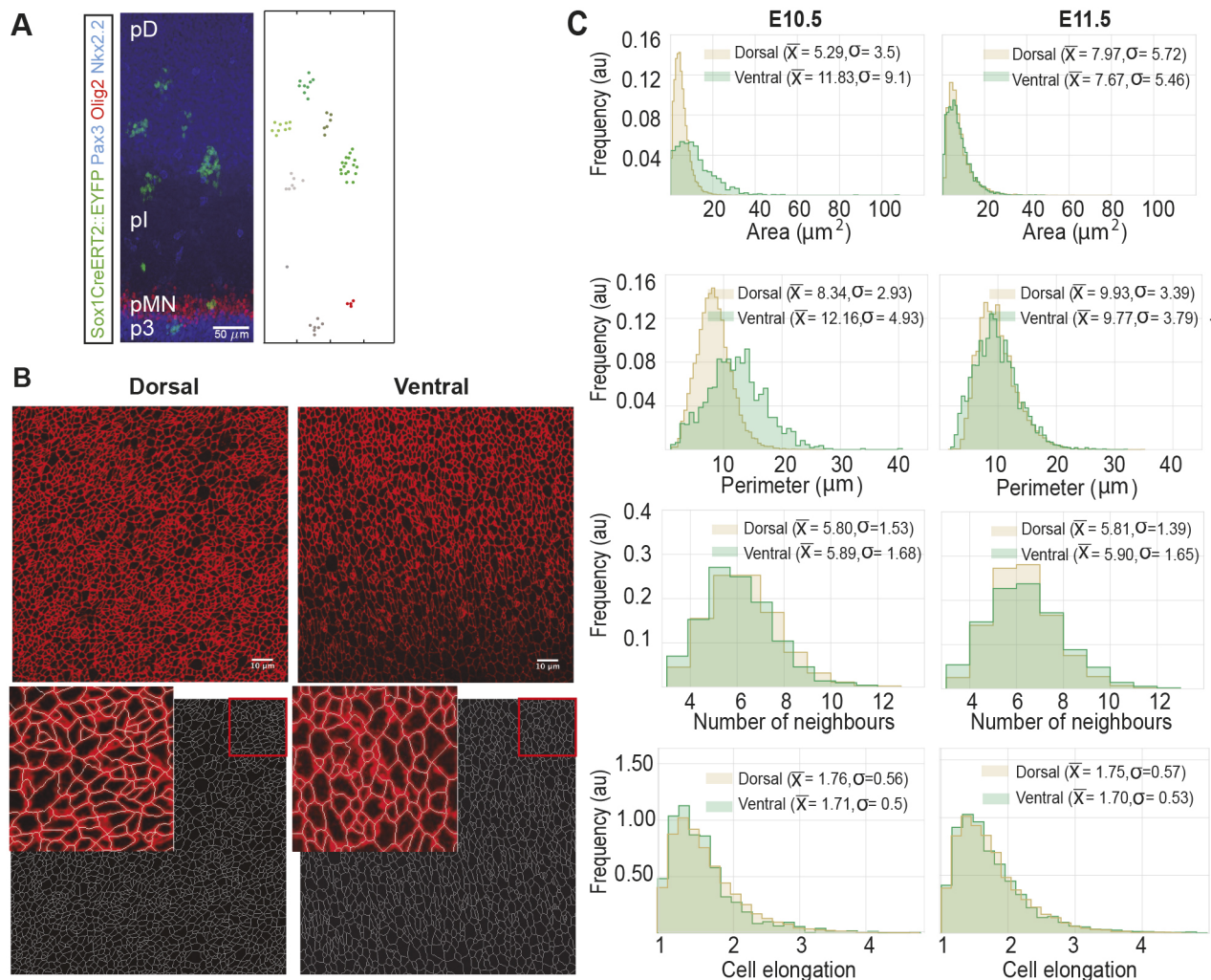
Fig. 1. Analysis of the cellular features of the mouse neuroepithelium. (A) Example clones in E11.5 embryos, data from Kicheva et al. (2014). Clonal labelling was induced at E9.5 of development. The coordinates of EYFP-labelled cells in the confocal image on the left are shown on the graph on the right. The AP/DV ratio of clones in the pMN domain (red marks) is higher than in the pD domain (green shades). Scale bar: 50 µm. (B) Top panels show the apical surface of E11.5 flat mounted mouse neural tube immunostained for ZO-1. Images were taken within the ventral (right) and dorsal (left) halves of the neural tube. Dorsal side up. Scale bar: 10 µm. Bottom panels show the segmented images after manual correction. Insets show an overlay of original and segmented image. (C) Histograms of apical area, perimeter, number of neighbours and elongation of cells from the dorsal (brown) and ventral (green) regions of E10.5 and E11.5 neural tubes. Sample sizes: E10.5, n=25 images of dorsal and five images of ventral domains from seven different embryos; E11.5, 11 images of dorsal, three images of ventral domains from three embryos.

in all domains was similar, the DV spread was not. Clones in all but the pMN domain were more elongated along the DV axis compared with the AP axis. By contrast, clones in the pMN domain have an average AP/DV ratio of ~1 indicating equal growth in DV and AP directions. This raises the question of what mechanisms operate to ensure equivalent AP growth across the tissue, while at the same time allowing for cell-type-specific differences in DV growth rates.

To address this, we developed computational tools to simulate the growth of the neuroepithelium and investigate the role of different mechanisms in the morphodynamics of the tissue. We made use of a representation of the apical 2D surface of the epithelium by employing a vertex model formalism (Nagai and Honda, 2001; Farhadifar et al., 2007; Smith et al., 2012; Fletcher et al., 2013). Vertex models have been used successfully to describe mechanical and molecular influences that determine the tissue growth and form of several epithelia (e.g. Farhadifar et al., 2007; Landsberg et al., 2009; Aegerter-Wilmsen et al., 2010; Wartlick et al., 2011; Trichas et al., 2012; Salbreux et al., 2012 and others) and we chose this

approach to test whether the experimentally observed variations in clone shape could be explained by the mechanics of the neuroepithelium. In these models each cell is represented as a polygon, the vertices and edges of which are shared between adjacent cells. The dynamics of a cell are described by the movement of its vertices, which are controlled by adhesive/tensile, contractile and repelling forces in and between cells.

To take account of the 3D configuration of the neural tube, we incorporated the effects of IKNM into the simulation framework. Using experimental data from the mouse neural tube, we then established model parameters for which simulations match in vivo observations. We used the resulting model to explore clonal shape within the neuroepithelium and the effect of spatially varying the differentiation rate within the tissue. Strikingly, we found that the increased differentiation rate of pMN progenitors is sufficient to explain the different shape of clones within the pMN domain. This indicates that the differences in clonal shape arise from differences in progenitor differentiation rates and global mechanical constraints,

and do not require polarised molecular signalling mechanisms. Simulations of the developing neuroepithelium using this model can contribute to our understanding of how tissue patterning and growth are controlled and coordinated.

RESULTS

Cell geometry in the mouse neuroepithelium

To construct a mechanical model of neural tube growth we first measured key features of neural progenitor organisation in the mouse embryonic neural tube. To this end, we imaged the apical tight junctions of the neural tube at forelimb level of E10.5 and E11.5 mouse embryos (Fig. 1B, top). The images were segmented, vertices and edges defined using 'Packing Analyzer v2.0' (Aigouy et al., 2010) (Materials and Methods; Fig. 1B, bottom).

Images from the dorsal half of the neural tube comprise the progenitors of dorsal interneuron subtypes, and we refer to this region as the pD domain. Images from the ventral half of the neural tube contain motor neuron and intermediate progenitor subtypes and we term this the pMN region (Methods). From the segmented images we determined the distributions of cell areas, cell perimeters, number of neighbours per cell and cell elongation (Fig. 1C). Cells in all samples had on average six neighbours as expected (Graustein, 1931; Classen et al., 2005; Gibson et al., 2006), with a standard deviation of ~1.5. There were some differences in the mean and variance of cell areas and perimeters in the samples (Fig. 1C), which were most noticeable at E10.5, when the rate of neuronal differentiation is highest in the pMN (Kicheva et al., 2014). Nevertheless, the average area of cells assayed in this way was consistent with previous measurements (Kicheva et al., 2014). Also, consistent with Lewis's Law, the relative average area of cells increases linearly with the number of cell neighbours (Fig. S1; Kokic et al., 2019 preprint). Using these data, we set out to develop an *in silico* model of the neuroepithelium.

A vertex model of the neuroepithelium including IKNM

We constructed a 2D vertex model of the apical surface of the neural tube in which cells are represented as polygons. The behaviour of each cell is governed by the movement of its vertices that follow a deterministic overdamped motion given the energetic contributions of cell elasticity, junctional forces arising from cortical contractility and the effect of cell-cell adhesion and cortical tension (Kafer et al., 2007; Lecuit and Lenne, 2007; Farhadifar et al., 2007; Hilgenfeldt et al., 2008; Landsberg et al., 2009; Aegerter-Wilmsen et al., 2010; Fletcher et al., 2014; Honda and Nagai, 2015; Alt et al., 2017). For the purposes of the simulation we developed custom Python code using an Euler method to solve the movement equation of each vertex, Eqn 4.

Topologically, the neural tube is a cylinder that grows at different rates along its AP and DV axes (Fig. 2A). Our analysis focuses on a region along the AP axis at the forelimb level. This region is relatively small compared with the entire length of the AP axis and is distant from the influence of the rostral and caudal limits of the neural tube. To take this into account and to avoid artefacts from introducing external boundary conditions, we used periodic boundary conditions in the AP axis by simulating the neural tube as a torus. Growth results in the circumferential and radial increase in the size of the torus over time. For visualisation we unwrapped the torus by cutting along both DV and AP axes to allow simulations to be rendered in 2D (Fig. 2A, bottom).

To describe the behaviour of neural progenitors within the simulation, a detailed description of cell growth, division and differentiation is required. Upon neuronal differentiation, cells lose

their apical attachments and are extruded basally from the epithelium (Fig. 2B, left). During each cell cycle, progenitors in the neuroepithelium undergo IKNM, in which their nuclei and the bulk cell volume translocate along the apical-basal axis of the neuroepithelium. Mitosis occurs at the apical surface of the epithelium. Nuclei move basally in G1 and undergo S-phase towards the base of the epithelium. During the G2-phase, nuclei migrate back to the apical surface for mitosis. A consequence of IKNM is that the apical area of cells, corresponding to the surface represented in the simulations, is affected by the cell cycle stage. When cells enter mitosis, they round up at the apical surface. This expands their apical area and compresses neighbouring cells. As a consequence, cells are likely to achieve their largest apical surface area in late G2 and M phase, and their smallest surface area in S-phase. The measured duration of cell cycle phases (Kicheva et al., 2014) (Table 1) can therefore be used to derive an approximation for the temporal changes in apical surface area of cells caused by IKNM.

To accommodate the effect of IKNM in our simulations we introduced a time-dependent target area function, $A_\alpha^0(t)$ (Eqn 1), which describes the desired apical area of the cell. This function depends on the age of the cell and the cell cycle phase and was constructed to account for the measured cell cycle dynamics:

$$A_\alpha^0(t) = \frac{1}{2}((t - t_0)g_\alpha + 1)(1 + (\rho_\alpha(t - t_0))^2), \quad (1)$$

where g_α is the growth rate of the cell α [for each cell this is chosen randomly from a normal distribution with a mean equal to the inverse of the life span of a cell (1/780 min) and a variance of 20% of the mean], t_0 is the moment when the cell α is born and $\rho_\alpha(t-t_0)$ represents the apical-basal position and depends on the phase of the cell cycle by a piece-wise linear function incorporating the dynamics of the cell cycle:

$$\rho_\alpha(\tilde{t}) = \begin{cases} 1 - \dfrac{\tilde{t}}{t_{G1}} & 0 \le \tilde{t} \le t_{G1} \\ 0 & t_{G1} < \tilde{t} \le t_{G1} + t_S \\ \dfrac{\tilde{t} - (t_{G1} + t_S)}{t_{G2}} & t_{G1} + t_S < \tilde{t} \le t_{G1} + t_S + t_{G2} \\ 1 & t_{G1} + t_S + t_{G2} < \tilde{t} \end{cases} \quad (2)$$

where t_{G1}, t_S and t_{G2} are the respective cell cycle phase durations and $\tilde{t} = t - t_0$. The position of a cell body along the apicobasal axis (see scheme in Fig. 2B, right) is given by the function $\rho_\alpha(t)$ where apical is 1 and basal is 0. The function $\rho_\alpha(t)$ is defined by four different straight lines which correspond to each cell cycle phase (Fig. 2C). In $G1$, the nuclear movement is from apical to basal and takes t_{G1} time and thus decreases linearly with time at rate $1-(t/t_{G1})$. During S-phase, the nucleus stays basal for time t_S, and $\rho_\alpha(t)$ is set to 0. Basal to apical migration occurs during $G2$, over the period t_{G2}, and is represented by the increasing function $\dfrac{t - (t_{G1} + t_S)}{t_{G2}}$. During mitosis, the function takes value 1. The functional form of $A_\alpha^0(t)$ is the product of a term which grows linearly in time, as we assume the volume of the cell does, and a term which interpolates between 1/2 and 1, as the cell moves from the basal to the apical surface, with a higher rate of increase as it approaches the latter surface.

Implemented in this way, the target area of a cell, which describes the desired apical area of the cell, takes account of both cell growth during the cell cycle and the position of the cell body along the
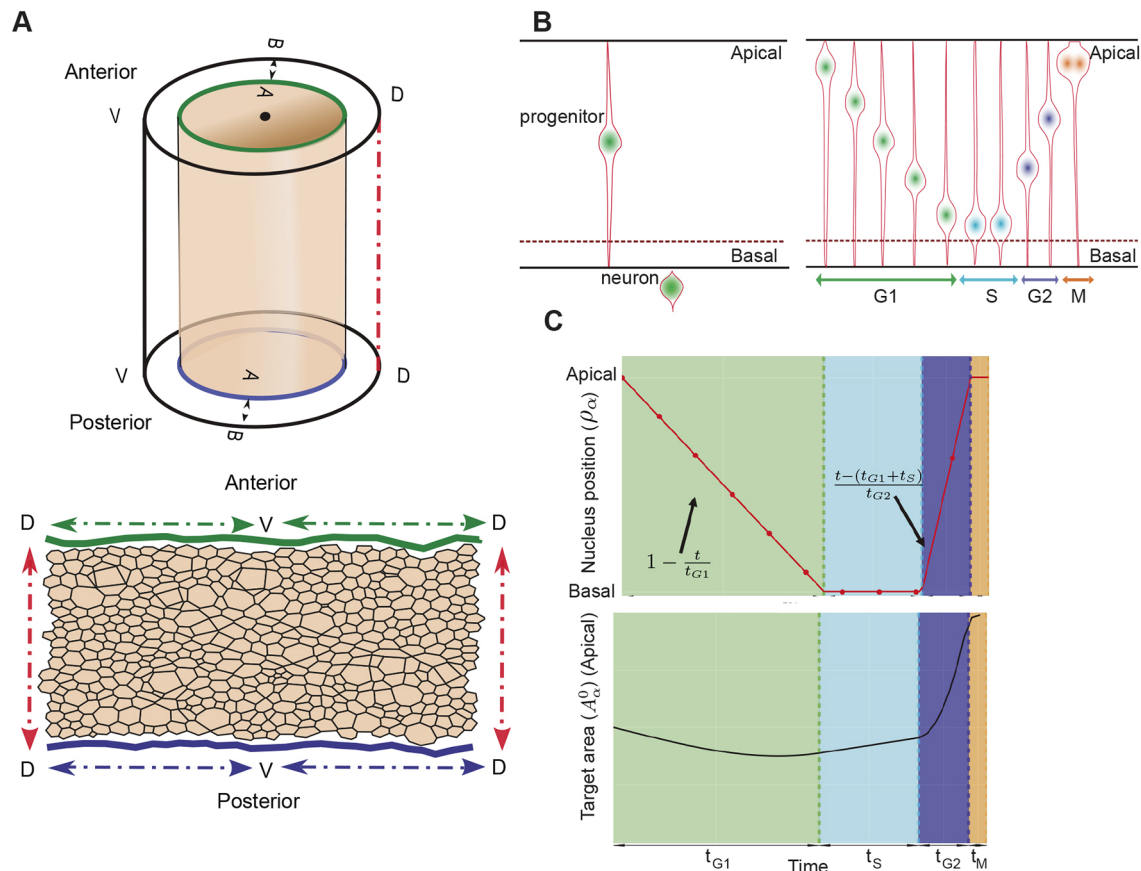
3

Fig. 2. Vertex model simulation framework for the neural tube incorporating interkinetic nuclear movement. (A) Top panel shows a 3D diagram illustrating the DV, AP and apical-basal (AB) axes on a cylindrical representation of the neural tube. Bottom panel shows a 2D polygon representation of the apical junctional network. In the simulations, periodic boundary conditions mean that the top-bottom and left-right edges are continuous. (B) Left panel represents the neuronal differentiation of a progenitor leading to loss of the apical contact and cell extrusion from the epithelium. Right panel represents IKNM: the apicobasal position of the nucleus changes with cell cycle phase. The nucleus moves basally during G1, undergoes S-phase basally, returns apically in G2 and is apical during mitosis. (C) Top panel shows a representation of the function used to describe nuclear position (ρ_α) during a simulated cell cycle. Bottom panel shows the apical target area that results from Eqn 1 during a cell cycle. Coloured regions in the top and bottom panels indicate different cell-cycle phase durations: t_{G1}, G1-phase (green); t_S, S-phase (light blue); t_{G2}, G2-phase (dark blue); t_M, M-phase (orange). This is an illustration for an example cell, the exact cell cycle behaviour of individual cells in simulations will vary.

apicobasal axis. It results in the apical area slowly reducing during G1, corresponding to the cell body moving towards the basal surface at the same time as the cell is growing, then increasing slowly during S-phase, rapidly expanding during G2, as the cell returns to the apical surface for division, and growing slowly during mitosis (Fig. 2C, bottom). In simulations we use the dorsal cell cycle phase times, indicated in Table 1, where t_S is 1/3 and t_{G2} is 2/3 of the S+G2 proportion time. Note that the target area given above is in nondimensional units. For the nondimensionalisation, see Materials and Methods, Vertex model implementation.

Division occurs when the cell is in M-phase ($\tilde{t} > t_{G1} + t_S + t_{G2}$) and the volume of the cell exceeds a critical value, A_c.

Table 1. Proportion of cells in the indicated cell cycle phases and total cell cycle time in minutes at stage E10 of cells in the ventral (V) and dorsal (D) region of the neural tube

Cell cycle phase	V	D
G1	0.7	0.4
S+G2	0.2	0.5
M	0.1	0.1
Total min	~780	~780

Data from Kicheva et al. (2014).

As a cell undergoes division two new vertices are created to form a new edge. One of these vertices is chosen as the midpoint of a randomly selected edge of the dividing cell with probability proportional to the edge length. The other vertex is the midpoint of the opposite edge, and if the cell has an odd number of sides, the second edge is the closer mid edge. The newly generated sister cells then commence the next cell cycle.

In the neural tube, newly generated neurons lose their apical attachments and delaminate basally (Fig. 2B, left). Hence, neuronal differentiation leads to the loss of cells from the plane of the neuroepithelium. In the simulation, this is achieved by identifying cells committing to differentiation, suppressing growth in these cells by assigning their target area equal to zero and allowing their area to decrease. As the area of a cell drops, some of its edges become small and disappear under certain T1 transition conditions (see below), which ultimately results in elimination of the cell. At the stage of development we are modelling, cells differentiate predominantly within the pMN domain. In simulations, we select cells to differentiate with a fixed probability per unit time.

The combined effect of cell growth, division and differentiation results in cells moving relative to each other, producing local remodelling of the epithelium and rearrangements of neighbouring

Table 2. Simulation constant parameters

Parameter	Meaning	Value	Ref
K	Elasticity coefficient	1 au	Farhadifar et al., 2007
A_c	Critical area	30 µm^2	-
T_1	Length threshold	0.048 µm	Kursawe et al., 2018
l_{new}	Distance new edge nodes after T_1	1.01 T_1	-
Δt	Time step	0.46 s	Fletcher et al., 2013
μ	Medium viscosity	0.276 K µm^2 s	-
μ'	DV drag viscosity	0.276 K µm^2 s	-
μ''	AP drag viscosity	13.8 K µm^2 s	-
λ	Proliferation rate	0.05 h^{-1}	Kicheva et al., 2014

cells. In the simulations, these topological rearrangements occur through T1 transitions. During a T1 transition an edge shorter than a prescribed length (chosen to be 3% of the average edge length in the tissue) is eliminated and a new edge of length l_{new} expands perpendicular to the old edge (values given in Table 2). However, if the rearrangement results in the formation of a two-sided cell, the cell is removed from the epithelium.

Simulation parameter estimation

We next used the experimental data to identify model parameters for which simulations match *in vivo* observations. The dynamics of the simulations are determined by the Hamiltonian (Eqn 5) that takes into account the energetic contributions of different cellular mechanical properties. The minima of this Hamiltonian can be described using two dimensionless parameters: $\bar{\Lambda} = \dfrac{\Lambda}{K(A^0)^{3/2}}$ and

$\bar{\Gamma} = \dfrac{\Gamma}{KA^0}$, where A^0 denotes the average of the target area, A_α^0, during the cell cycle (Farhadifar et al., 2007). This average value was obtained as the mean value of the target area across all cells at the end of 12 simulations and was 1.25 nondimensional units. In the standard implementation of the model this leads to a phase diagram describing four different parameter regions in which the tissue has different biophysical properties, (Supplementary Materials and Methods, section II; Farhadifar et al., 2007; Magno et al., 2015).

Similar to some previous studies (Canela-Xandri et al., 2011; Kursawe et al., 2018), the target area term of the Hamiltonian we used includes a cell cycle dependent component. However, as vertex movement is substantially faster than the cell cycle, the same phase diagram remains applicable (for more details of the derivation of the phase diagram see Supplementary Materials and Methods, section II).

We focus our attention on the region of the phase diagram exhibiting epithelial properties (Regions II and III in Fig. S10); this is given by the following relation between normalised tension and contractility parameters, (Magno et al., 2015):

$$-\frac{\bar{\Lambda}}{4\sqrt{2}3^{1/4}} < \bar{\Gamma} < \frac{2 - 3\sqrt[6]{3}\bar{\Lambda}^{2/3}}{8\sqrt{3}}. \qquad (3)$$

To narrow down the region of parameter space $(\bar{\Lambda}, \bar{\Gamma})$ relevant for neural tube simulations, we systematically screened parameter sets to identify those that generated cell geometries comparable with experimental data. We compared experimental and simulated empirical cumulative distribution functions (ECDF) of area, perimeter, number of cell sides and cell elongation (defined in Materials and Methods, Experimental data analysis) and values of standard deviation of area and perimeter. We used experimental data from E11.5 dorsal neural tubes compared with the ECDF obtained from vertex model simulations with different combinations of

$\bar{\Lambda}$ and $\bar{\Gamma}$. Assessing the match between experimental and simulation data indicated a diagonal region in parameter space for which all the measured features of the *in silico* cell geometries closely matched those observed *in vivo* (Fig. 3A). The shape of this region is similar to previously published vertex model simulations (Kursawe et al., 2018). Moreover, the agreement with experimental data was better in the model with IKNM (Fig. 3A), compared with a standard model formulation without IKNM in which the target area is constant over time (Fig. S2). Therefore, in subsequent simulations we used the model with IKNM and six parameter sets selected from different locations from within the region of parameter space representing the best agreement with experimental data.

Simulating anisotropic tissue growth

We next turned our attention to the overall tissue growth. Our previous experimental studies (Kicheva et al., 2014) indicated that the tissue grows asymmetrically in DV and AP directions. During the period under consideration, the DV length of the tissue increased more than the AP length. This effect was reflected in the shape of clones of lineage-related cells, such that the mean ratio of AP to DV spread of the clones outside of the pMN domain was ~0.3 (Kicheva et al., 2014).

In the simulations, expansion along the DV and AP axes is resisted by drag forces that have coefficients μ' and μ'', respectively. A difference between these two coefficients generates different rates of DV and AP tissue growth and consequently alters the tissue AP/DV aspect ratio (Figs S3,S9; Supplementary Materials and Methods, section I), imitating the effect of physical constraints on *in vivo* tissue expansion. For all six selected $\bar{\Lambda}, \bar{\Gamma}$ parameter sets, we identified a range of values of μ' and μ'' that were consistent with both the experimentally observed AP/DV aspect ratio and reduction of the DV length of the pMN domain (Fig. 3B; Fig. S3A). Within this range of dimensionless values, the values μ'~0.02 and μ''~1 matched closely the AP/DV ratio of 0.3 (Fig. S3B) and were used in further analysis.

To test the effect of these asymmetric forces, we examined the shape of clones in simulations by tracking lineage-related cells *in silico*. For this, simulations were started from a field of 100 cells and run for 30 h of biological time to allow the simulation to equilibrate. Following this initialisation period, the progeny of individual cells were tracked for a further simulated 48 h. This corresponds to an average of 3-4 cell divisions, mimicking the experimental conditions in which the *in vivo* clonal data were generated. Similar to the experimental data, *in silico* lineage-related cells (clones) tended to form coherent groups and the shape of clones was similar between experiments and simulations (Fig. 3C,D). For all six parameter sets, cells within a clone tended to spread more along the DV axis compared with the AP axis to give an *in silico* AP to DV aspect ratio of ~0.3 (Fig. 3D), similar to clones in the mouse neural tube (Kicheva et al., 2014). Thus, with the identified parameters, there was a good correspondence between the behaviour of cells in the simulation and those in the real neuroepithelium.

The rate of neuronal differentiation affects the shape of progenitor clones

Clones in the pD domain have a lower AP/DV aspect ratio than clones in the pMN domain. Having established a simulation framework and identified parameters that mimic neuroepithelial behaviour, we set out to address what could account for the difference in clone shape between domains. Progenitors within the pMN differentiate at a substantially higher rate than other progenitors at this stage of development (Kicheva et al., 2014), raising the possibility that this accounts for the difference in clone shape.
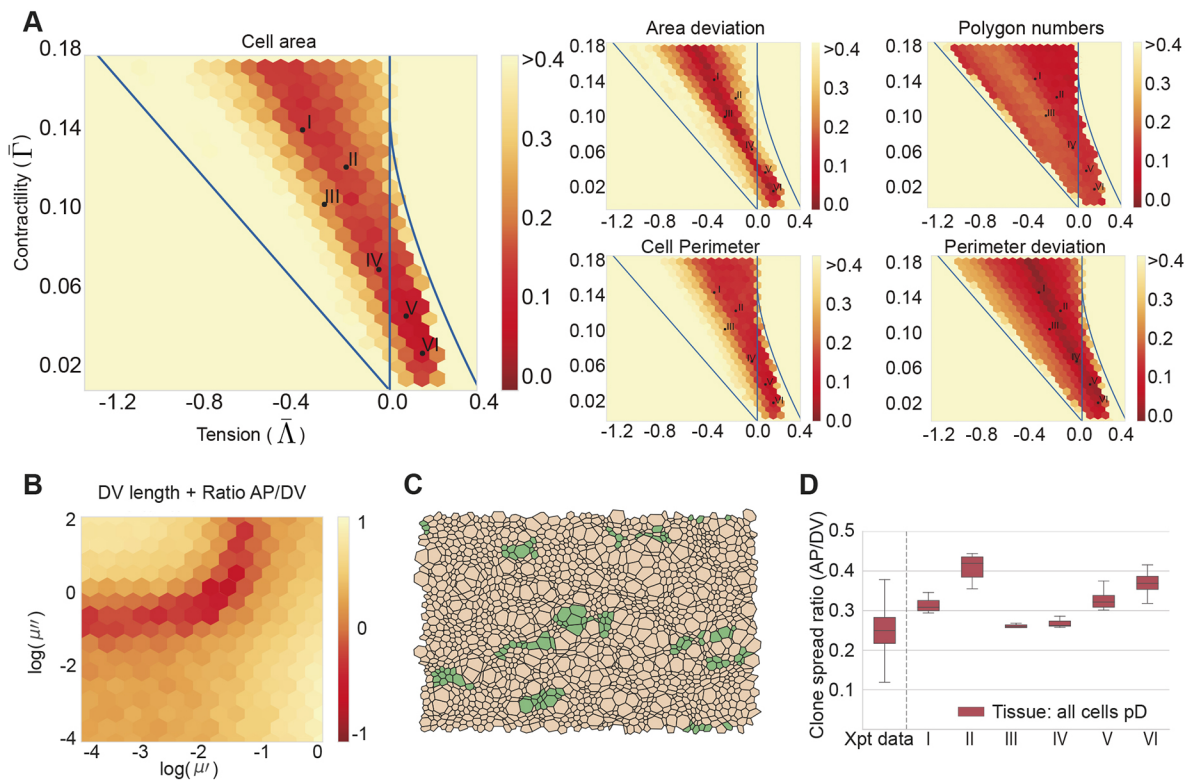
Fig. 3. Identification of simulation parameters matching experimentally determined features of the neuroepithelium. (A) Similarity of experimental data and simulations with the indicated composite tension and contractility parameters. Colour code represents the average of the maximum distance of the empirical cumulative distribution function for cell area, cell perimeter and polygon number, and the absolute difference between the standard deviations of cell area and cell perimeter (see Materials and Methods). Experimental data is from E11.5 embryos and simulations correspond to 10 independent simulations per point in parameter space. Roman numbered dots indicate the mechanical parameters selected to study clonal distribution, $(\bar{\Lambda}, \bar{\Gamma})$: I, (−0.4, 0.14); II, (−0.2, 0.12); III, (−0.3, 0.1); IV, (−0.05, 0.065); V, (0.075, 0.04); VI, (0.15, 0.02). μ' and μ'' are 0.02 and 1, respectively. Blue lines demarcate the four different parameter regions of the phase diagram (see Supplementary Materials and Methods, section II). (B) Heatmap as in A, but the absolute value of the difference (log scale) in the change in DV length of the tissue over 48 h plus the absolute value of the difference in the final tissue aspect ratio (AP/DV) between simulations and experimental data was taken and this quantity was averaged over 10 simulations for each point. $(\bar{\Lambda}, \bar{\Gamma})$ used for these simulations are from the mechanical parameter set V. (C) Examples of the shape of simulated clones tracked over 48 h demonstrate the DV bias in their elongation *in silico*. Brown represents pD cells, green represents clones of pD cells. (D) Comparison of clone spread ratio (AP/DV) between experiments (Xpt data) and simulations. Box plot shows the quartiles of 12 realisations of the simulation with no differentiation (all cells pD domain); median values (middle bars) and interquartile ranges (boxes); whiskers extend from the box to show the range of the data 1.5x the interquartile range past the first and third quartiles. Roman numerals indicate mechanical parameters used $(\bar{\Lambda}, \bar{\Gamma})$ in A. Other parameter values are provided in Table 2.

We implemented a pMN domain in simulations by defining a region of tissue with an appropriate differentiation rate. Following the initialisation period, a pMN domain comprising 30% of DV length of the neural tube was introduced by imposing a differentiation rate of 0.1 h^{-1} on cells in this region, corresponding to the maximum differentiation rate of pMN progenitors *in vivo* (Kicheva et al., 2014). The remainder of the tissue was designated as pD domain and lacked differentiation, representing the more slowly differentiating dorsal progenitor domains *in vivo*. Simulations were continued for a further period equivalent to 48 h of biological time (Fig. 4A).

At the end of the simulations, the proportion of tissue composed of the pMN decreased from the initial 30% DV length of the tissue to ∼5% DV length for all six mechanical parameter regimes (Fig. 4A; Fig. S4A). This is a consequence of the increased differentiation rate resulting in a loss of progenitors from the pMN. This decrease in the DV extent of the pMN matches the experimentally observed reduction in the DV proportion of the neuroepithelium occupied by the pMN domain from 30% of the neural tube at E9 to 5% 48 h later at E11 (Kicheva et al., 2014) (Fig. S4A). Moreover, clones in the pD domain comprised 8-12 cells on average, consistent with an average of 3-4 cell divisions that occur in the 48 h period (Fig. 4B; Movie 1). By contrast, pMN clones contained 4-5 cells per clone. These *in silico*

clone sizes are consistent with the clone sizes observed in the experimental data (Fig. 4C). Together these data indicate that the behaviour of the simulated pMN and pD domains matches the behaviour observed *in vivo*.

We then examined the spread of clones along the AP and DV axes (Fig. 4D). Similar to the simulations lacking a pMN domain (Fig. 4D), clones within the pD region were anisotropic with an AP/DV aspect ratio of ∼0.3. By contrast, for all six parameter sets, clones within the simulated pMN domain had a substantially higher AP/DV aspect ratio ($P<0.05$, two-sided *t*-test, Fig. 4D). The marked difference between the AP/DV aspect ratio of the pMN and pD domains was seen in both experiments and simulations, independent of the number of cells in a clone (Fig. S5). These results reveal that the difference in the shape of clones in the pMN compared with the rest of the neural tube can be explained by the increased differentiation rate of these cells.

The anisotropy of tissue growth depends on the net growth rate

To investigate how the increased rate of differentiation affects the anisotropy of tissue growth, we analysed how tissue anisotropy changed when different differentiation rates (0-0.1 h^{-1}) were
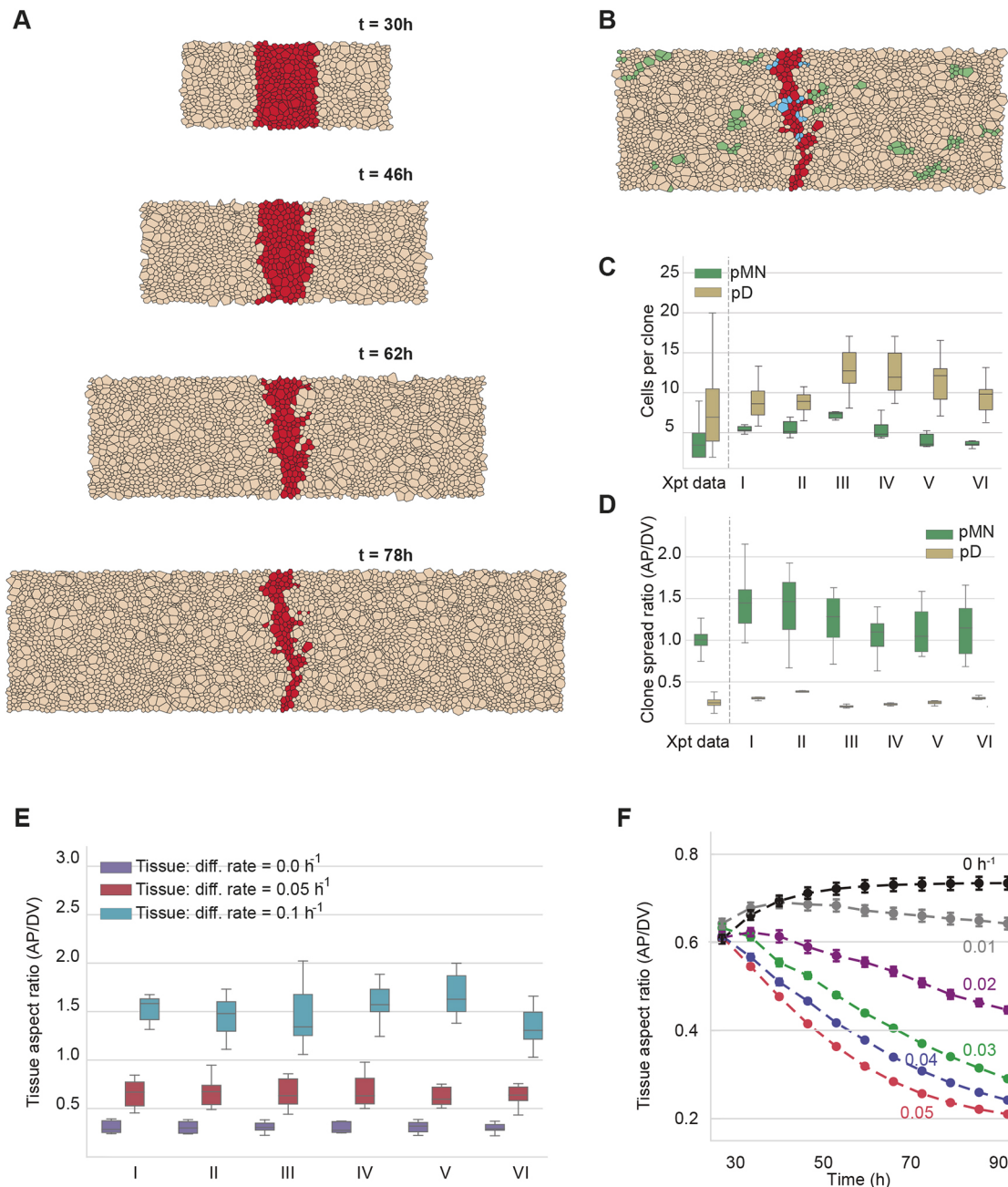
Fig. 4. The rate of neuronal differentiation affects the anisotropy of tissue growth. (A) Snapshots from a simulation of a tissue with pD (brown) and pMN (red) populations. Differentiation in the pMN domain is initiated at 30 h, after which the relative DV length of the pMN domain decreases from 30% to 5% over 48 h. (B) Examples of clones tracked during the 48 h simulation *in silico*. Brown represents pD cells, green represents clones in pD domain, blue represents clones in pMN domain, red represents pMN cells. (C) Comparison of number of cells per clone between experimental data (Xpt data) and simulations in pMN (green) and pD (brown). (D) The ratio of AP/DV spread of clones in the pD (brown) and pMN domain (green) domains compared with experimental data (Xpt data). (E) Tissue aspect ratio (AP/DV) for simulations of homogeneous tissues consisting of a single cell type with the indicated differentiation rates: 0 h^{-1} (purple), 0.05 h^{-1} (red) and 0.1 h^{-1} (light blue). (F) Tissue aspect ratio (AP/DV) over time of simulated tissues with the indicated proliferation rates and differentiation rate equal to zero for a given regime V. Box plots show median values (middle bars) and interquartile ranges (boxes); whiskers extend from the box to show the range of the data 1.5x the interquartile range past the first and third quartiles. Data in C-F is derived from 12 different simulations per parameter set and Roman numerals indicate the mechanical parameters $(\bar{\Lambda}, \bar{\Gamma})$ from Fig. 3A. Differentiation rate in pMN for A,B,C and D is 0.1 h^{-1}. Other parameters are indicated in Table 2.

imposed uniformly throughout the tissue. This revealed that a higher differentiation rate correlated with a larger AP/DV aspect ratio of the tissue (Fig. 4E). This effect is consistent with the observation that a higher differentiation rate correlates with a higher AP/DV aspect ratio of clonal shape (Fig. 4D; Fig. S6). Furthermore, this tendency was present for all ratios of μ''/μ' larger than one (Fig. S7). This indicates that as long as there are global anisotropic drag forces, the

differentiation rate determines the exact extent of tissue growth anisotropy, with higher differentiation rates yielding higher AP/DV aspect ratios.

The decreased anisotropy of clones of cells in the pMN domain might result from the decreased net growth rate of the pMN, rather than directly from the increased differentiation. To investigate the effect of tissue growth rate on anisotropy, we began by further

simplifying the problem and constructing a simple model in which we assumed cells were identical and rectangular (Supplementary Materials and Methods, section III). This predicted that the aspect ratio tends asymptotically to a value that depended on the drag coefficients and the growth rate. For very slow growth of the tissue (low net proliferation rate), the aspect ratio would be close to one, whereas for very rapid growth, it would be close to the square root of the ratio of drag coefficients (Supplementary Materials and Methods, section III). Thus, the effect of the drag on tissue anisotropy would be less pronounced for slow growth rates, leading to more isotropic growth. To test this hypothesis, we ran simulations without differentiation but with varying proliferation rates (Fig. 4F). Consistent with our hypothesis, the slower proliferation rates decreased the anisotropy of tissue growth. Thus, increased differentiation per se was not necessary for the observed behaviour. Instead, the net growth of tissue affects its aspect ratio.

Further investigation showed that the effect of differentiation rate on the aspect ratio of the tissue was more complex than simply slowing the effective tissue growth. Although both increasing the differentiation rate and decreasing the proliferation rate correlated with decreasing tissue growth anisotropy at a given time (Fig. S6A-F), the anisotropy that corresponded to a specific net growth rate was not always the same. Instead, different degrees of anisotropy were achieved for the same net growth rate, depending on whether proliferation or differentiation was modulated (Fig. S6F). Furthermore, tissues of similar size (generated by similar net growth rates) would adopt different aspect ratios depending on the relative contributions of proliferation versus differentiation to the net tissue growth (Fig. S6A-F). Tissues that differentiate have increased anisotropy (lower AP/DV ratio) compared with tissues that reach the same size without differentiation (compare Fig. S6G and S6H). We postulate that increasing differentiation rate facilitates the rearrangement of internal boundaries which allows the tissue to tolerate more tissue growth anisotropy. Consistent with this, a high differentiation rate $(0.1\,h^{-1})$ increased the frequency of T1 transitions (to 0.38 ± 0.04 per cell per h by the end of the simulation) compared with simulations with no differentiation (0.14 ± 0.03 per cell per h). Thus, differentiation has opposing effects: it slows growth, which tends to make growth more isotropic (Supplementary Materials and Methods, section III shows that if cells cannot rearrange, the final anisotropy of the tissue increases with the exponential growth rate of cells) and it facilitates internal boundary rearrangements, which tends to allow tissue growth to be more anisotropic (Supplementary Materials and Methods, section III shows that if cells are free to rearrange to become individually isotropic, the total energy is independent of the tissue aspect ratio, which is therefore primarily controlled by the anisotropic drag). Further work will be needed to fully understand the determinants of tissue aspect ratio.

We next turned our attention to the cellular dynamics that result in the anisotropic growth of the tissue. We first measured the orientation of T1 transitions. In the pD domain, the orientation of a T1 transition more frequently resulted in topological rearrangements that replace an AP-directed edge with one in the DV direction (Fig. 5A). Such transitions cause cells to intercalate, expanding the DV axis. There was no such bias in cells of the pMN domain. A consequence of these dynamics was a change in the orientation of cells. Measurements of cell elongation, defined as the square root of the ratio of the eigenvalues of the second moment matrix of the vertices of the cell (Materials and Methods), indicated that cells were equally elongated in the pMN and pD domains (Fig. 5B). However, in the pD domain cells tended to be orientated with their long axis in the DV direction,

whereas cells in the pMN domain tended to be orientated with their long axis in the AP direction (Fig. 5C). Strikingly, these differences in cell orientation between cells in the dorsal and ventral halves of the neural tube were also observed in the experimental data (Fig. 5C). This change in cell orientation resulted in a difference of the mean DV length of cells, with pD cells having approximately 10% larger DV lengths than pMN cells in both simulations and experiment (Fig. 5D). Thus, the change in cell shape alone had a minor contribution to anisotropic tissue growth, suggesting that T1-mediated cell rearrangements is the main factor driving the DV extension of the tissue.

In contrast to the bias in cell rearrangements, the axes of cell divisions in our simulations were distributed uniformly in both the pD and pMN domains (Fig. 5E,F) indicating little, if any, bias in division orientation. In the simulations this is a consequence of mitotic cells markedly reducing their elongation, allowing for random orientation of the division angle (Fig. S8). To test whether this was consistent with the *in vivo* observations we examined the orientation of mitotic spindles in anaphase cells, as a proxy for the orientation of cell division at E10.5. This revealed a uniform distribution of cell division orientation in both dorsal and ventral regions of the neural tube (Fig. 5F). Together these results suggest that a difference in cell rearrangements, rather than oriented cell division, account for the reduction of anisotropic tissue growth in the pMN domain.

In summary, the experimental observations are consistent with a model in which tissue growth is resisted by forces which are larger in the AP direction, causing anisotropic growth of the tissue. This effect is lessened in slow-growing epithelia. Thus, clones in the rapidly growing pD domain become more anisotropic after a fixed period of time than clones in the more slowly growing pMN domain. When the tissue grows anisotropically, it does so by biasing the direction of T1 transitions, rather than by biasing the orientation of cell divisions.

DISCUSSION

To understand the mechanisms by which tissue pattern, mechanics and growth are coupled in the vertebrate neural tube, we used experimental data to construct a mechanical model of the developing neuroepithelium. This allowed us to explore how proliferation and differentiation of individual cells, together with global mechanical constraints, influence the spatiotemporal dynamics of pattern formation in the tissue. Previous observations indicated that there are differences in the anisotropy of the shape of clones in different DV regions of the neural tube (Kicheva et al., 2014), however, how this anisotropy emerged was not understood. Our simulations and analysis indicate that, in the presence of global mechanical constraints, local differences in growth rate create local differences in the anisotropy of tissue growth, consistent with experimental observations. The analysis suggests an explanation for how an isotropic process, such as cell differentiation, can affect an anisotropic process, such as the direction of clonal expansion, given that global mechanical properties (here, dissipation) are anisotropic.

We adopted the well-established vertex model framework to describe neuroepithelium growth (Nagai and Honda, 2001; Farhadifar et al., 2007; Smith et al., 2012; Fletcher et al., 2013). It provides a scalable and computationally efficient means to understand how tissue morphogenesis is influenced by the combined effect of cell shape, forces generated by growing cells and external mechanical constraints. However, one of the challenges of modelling the neural tube epithelium resides in the 3D dynamics of neural progenitors. Similar to many pseudostratified epithelia, cells
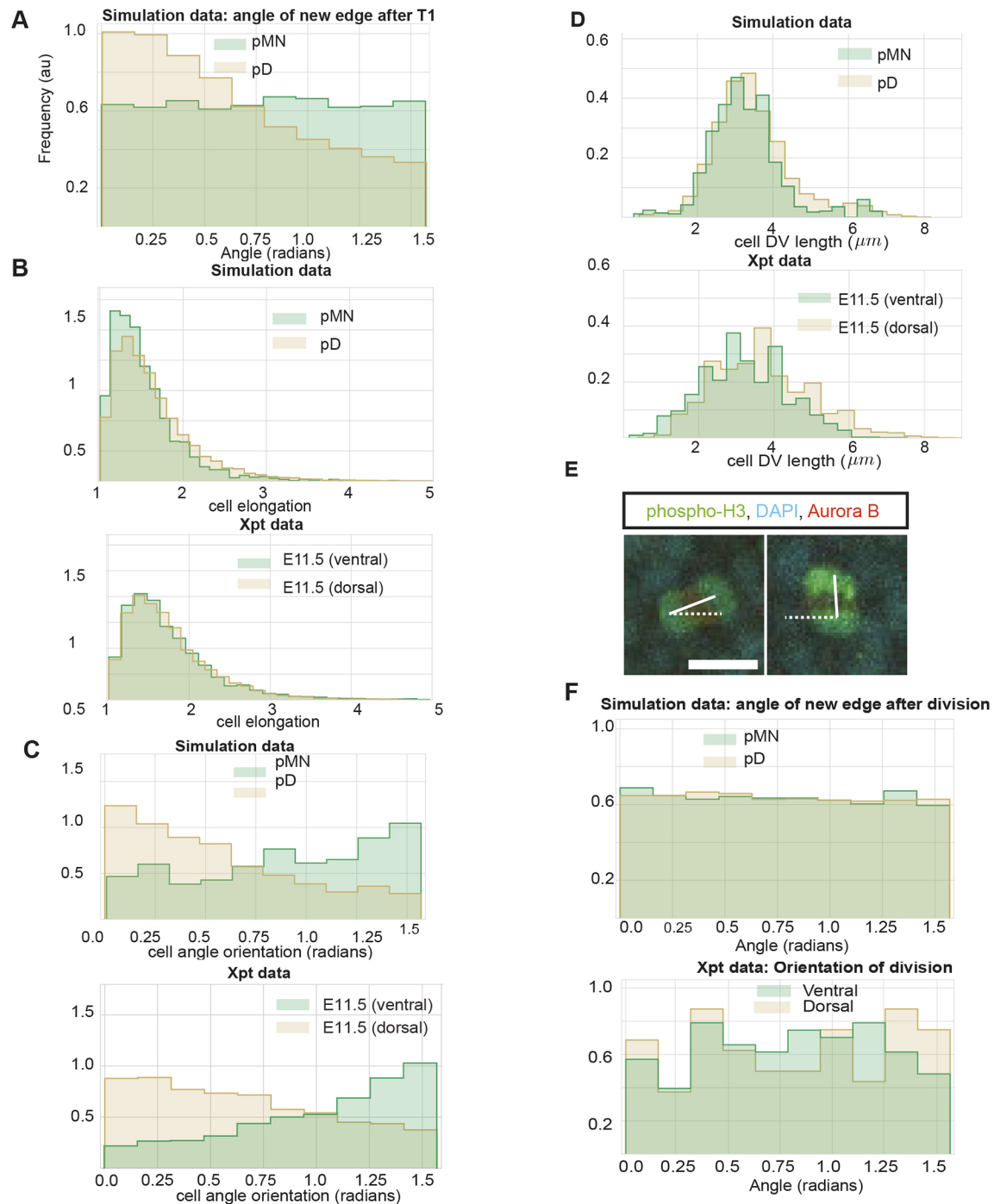
Fig. 5. Contribution of cell rearrangements, cell shape and cell division orientation to anisotropic growth. (A) Orientation angle with respect to the DV axis of the newly formed edge after a T1 transition in the pMN (green) or pD (brown) domains. (B) Distributions of cell elongation in simulations and experimental data at E11.5. (C) Distributions of the orientation angle of the long axis of cells with respect to the DV axis in simulations and experimental data at E11.5. (D) Cell DV length distribution calculated by taking the vertex coordinates and calculating min(x)-max(x) (x-axis represents DV direction) in simulations and experimental data in the indicated regions. (E) The angle of cell division orientation *in vivo* as outlined by the white lines in two example cells was measured at E10.5. Dotted line indicates AP axis. Scale bar: 10 µm. (F) Distributions of cell division orientation in simulations and experimental data in the indicated regions. Angle is represented by radians where 0 is parallel to the DV axis. The angle of the new edge after cell division should be roughly orthogonal to the axis of cell division. For simulations, distributions were estimated after 12 realisations using mechanical parameter regime V. Differentiation rate in pMN domain 0.1 h^{-1}. Other parameters are indicated in Table 2. For experimental data, distributions were calculated at E11.5. Eleven images of the dorsal and three images of the ventral domain from three embryos were used in B,C,D and F.

within the neuroepithelium undergo IKNM (Sauer, 1935) in which cell nuclei migrate between the apical and basal surfaces in synchrony with the cell cycle. Previous approaches have introduced a time dependence to the target area (Canela-Xandri et al., 2011; Kursawe et al., 2018) and we extended the formalism by including the effect of the IKNM and cell cycle on the preferred target apical area. This allowed us to determine mechanical parameters from experimental images of the apical plane, without requiring 3D reconstruction of the

neural tube. We could thus recapitulate properties of the pseudostratified dynamics of the tissue without compromising the computational efficiency of the model.

To identify the mechanical parameters of the model, we varied the cell tension, contractility and dissipative forces and compared descriptors of cell and tissue geometry in the resulting simulations with experimental data. The parameter values that produced the highest correlations with experimental data reside in the region of parameter space in which the unperturbed ground state is represented by hexagonal packing (Nagai and Honda, 2001; Gibson et al., 2006; Farhadifar et al., 2007; Magno et al., 2015) and there is a negative correlation between tension and contractility. This is as expected (Kursawe et al., 2018) and in line with parameters used in previous epithelial vertex models (e.g. Farhadifar et al., 2007). Importantly, a model without IKNM yielded a different set of parameters (Fig. S2A) and a poorer correlation with the experimental data (Fig. S2B).

A notable property of neural tube growth, observed in the brachial region at E11.5 of mouse development, is that most of the tissue extends faster in the DV direction than in the AP direction (Kicheva et al., 2014). We found that cell divisions do not show a preferred orientation in the epithelial plane, hence this anisotropy of tissue growth must arise from mechanical constraints. To model this, we assumed that the overall growth of the tissue was resisted by drag forces with different coefficients in the two directions. In general, the sources of resistive forces in epithelia are poorly understood (Alt et al., 2017). In the neural tube, it is possible that expansion is mechanically constrained by the adjacent tissues. Thus, the laterally located somites might affect radial expansion, whereas the process of axis elongation through the addition of cells to the caudal end of the neural tube (Bénazéraf et al., 2010; Mongera et al., 2018) might contribute to forces acting in the AP direction. Obtaining mechanical measurements, such as tension and pressure, using force inference methods (Chiou et al., 2012) within the mouse neural tube *in situ* might provide insight; however, assaying these properties *in vivo* without surgical disruption is difficult or impossible. Similarly, the inaccessibility to live imaging of the unperturbed apical surface, which forms the internal face of the intact neural tube, remains a challenge that hinders obtaining kinematic data on cell shape and movement. Nevertheless, imposing asymmetric drag forces in the simulations generated predictions concerning cell shape, the orientation of the major axis of cells and cell division orientation that were borne out by the experimental data (Fig. 5).

Although the nature of the resistive forces warrants further investigation, the simulations revealed that the anisotropic growth of the tissue resulted from cell rearrangements, rather than changes in cell shape. Thus, T1 transitions were preferentially oriented such that it was more likely for an edge in the AP direction to be replaced by one in the DV direction (Fig. 5A) and the cell intercalation that resulted from T1 transitions contributed to the tissue extension in the DV direction.

Encouraged by the similarity between simulations and experimental data, we used the model to examine the clonal spread in different progenitor domains. The shape of clones was anisotropic throughout most of the neural tube, but clones in the pMN domain were smaller and rounder (Kicheva et al., 2014). The pMN domain is distinguished by a high rate of progenitor loss due to terminal differentiation (Ericson et al., 1992; Kicheva et al., 2014; Sagner et al., 2018), which causes the smaller clone sizes. However, the basis for the difference in clone shape was unclear. pMN cells are molecularly distinct from other progenitors and one possibility was that cell orientation or arrangement was under local molecular control. For example, pMN progenitors express different sets of

adhesion molecules than adjacent domains (Rousso et al., 2012), raising the possibility that cell-cell communication plays a role in shaping the pMN domain. Strikingly, however, the model showed that the experimentally observed anisotropy in tissue growth could be reproduced simply by the increased differentiation rate of pMN progenitors in conjunction with the global difference in the resistive forces in AP and DV directions. The difference in resistance causes the tissue to become increasingly more anisotropic with time. Furthermore, increasing the differentiation rate or decreasing the proliferation rate causes the tissue to grow more slowly and become less anisotropic over a given period of time. Hence, the net growth rate is a governing factor that influences the degree of anisotropy, with slow growth being more isotropic.

We found that this change in tissue shape anisotropy over time not only depends on the overall growth rate of the tissue, but also on the relative magnitudes of the proliferation and differentiation rates. Increased differentiation, which removes cells from the epithelium, facilitates cell rearrangements and effectively increases the fluidisation of the tissue (Ranft et al., 2010). This alters the degree of anisotropy that is achieved for a given tissue size compared with growth without differentiation. In summary, the difference in the growth regime between domains influences the degree of tissue anisotropy. Further theoretical investigation will be needed to understand the exact relationships between growth anisotropy, the rate of proliferation and differentiation.

Our analysis shows that the orientation of cell divisions in experimentally observed tissues, as well as in simulations, is random. This suggests that cell division orientation does not contribute to anisotropic tissue growth (Bittig et al., 2008; Li et al., 2014). A surprising observation in our data is that, despite preferential cell elongation in the DV direction, cell division orientation is apparently random in the AP/DV plane; this could be explained by the decrease in elongation observed in mitotic cells (Fig. S8). Cell division has been found to be frequently oriented along the longest planar axis of a cell (Baena-López et al., 2005; Mao et al., 2011; Wyatt et al., 2015; Seldin and Macara, 2017 preprint), although this is not always the case and external and internal cues can determine the orientation of cell division in a shape-independent manner (Gong et al., 2004; Bowman et al., 2006; Konno et al., 2008; Gillies and Cabernard, 2011; Bosveld et al., 2016; Finegan et al., 2019). In the spinal cord, the plane of cell division is regulated along the apicobasal axis and is accompanied by rotations of the metaphase plate (Morin et al., 2007). This regulation is important for maintaining the integrity of the epithelium. Our data are consistent with the idea that the apicobasal orientation of the spindle is the dominant mode of regulation in the spinal cord, with no specific mechanism acting to orient the planar angle. It could be that the random orientation of divisions in the epithelial plane and the decoupling from cell shape is necessary to achieve efficient apicobasal orientation (Morin et al., 2007). Further studies will be necessary to investigate this thoroughly.

A consequence of the difference in clone shape between pMNs and other progenitor subtypes is that cells in all progenitor domains expand at equal rates along the AP axis, despite the overall smaller size of pMN clones. Thus, there is no net AP movement between progenitor domains and cells stay in register as development proceeds. This means that cells in different DV domains with the same AP identity remain adjoining. As AP identity is established early during neural development, maintaining position relative to other cells in the epithelium may be important for the later assembly of position-appropriate functional neuronal circuits.

In conclusion, we described a vertex model of a pseudostratified epithelium and used it to study the growth of the neural tube and

how cell differentiation influences clone shape. In future work, we wish to couple this tissue model to quantitative descriptions of the spread of morphogens that pattern the tissue and the gene regulatory networks that specify neuronal subtype identity. In this way, we hope to gain insight into the coupling of growth and patterning in the neural tube and understand how the position, precision and proportions of cell types are achieved.

MATERIALS AND METHODS
Experimental data analysis
All animal procedures were performed in accordance with the Animal (Scientific Procedures) Act 1986 under the UK Home Office project licences PPL80/2528 and PD415DD17. E10.5 and E11.5 mouse embryos were collected and processed for dissection, fixation, immunostaining and flat-mounting as previously described (Kicheva et al., 2014). Primary antibodies used were: mouse anti-ZO-1 (33-9100, Zymed Laboratories, 1:100), rabbit anti-phospho Histone H3 (06-570, Millipore, 1:1000), mouse anti-Aurora B (AIM1, BD Transduction Laboratories, 1:500), rabbit anti-Olig2 (AB9610, Millipore, 1:1000) and mouse anti-Pax3 (AB_528426, DSHB, 1:20). For the experimental clone shapes, we re-analysed the data in Kicheva et al. (2014). Cell elongation was calculated from the second moment matrix of the polygon representing the cell by taking the square root of the ratio of the largest to the smallest eigenvalue. Cell angle orientation was defined by $arctan(x1/y1)$, where $x1$, $y1$ represent the AP and DV component of the eigenvector corresponding to the largest eigenvalue.

To quantify the cell division angle, E10.5 embryos were stained with DAPI, phospho-H3 and Aurora B to mark dividing cells, and Pax3 and Olig2 to mark the dorsal and pMN domains, respectively. Spindle rotation ceases in anaphase (Morin et al., 2007). Cells in this phase were identified by low levels of phospho-H3, separated sister chromatids and Aurora B staining associated with the central spindle and only these cells were considered for the analysis (Fig. 5B, bottom). The orientation of the chromosomes with respect to the AP axis of the embryo was measured.

For the analysis of cell geometries, we used images of flat-mounted embryos of approximate size 80×80 μm. Images taken within the dorsal half are composed of Pax7+ pD progenitors, whereas images taken in the ventral part of the neural tube contained up to 50% pMN cells with the remainder being progenitors of the p2-p0 domains. Images were processed using the Fiji plug-in 'Packing Analyzer v2.0' (Aigouy et al., 2010), which segments the image, classifies cell edges and vertices, and measures cell areas, perimeter and neighbours. Segmentation mistakes were manually corrected.

Vertex model description
Cells are represented as polygons with straight edges connecting vertices. Cells are enumerated by $\alpha=1, \ldots, N_c$ and vertices are enumerated by $i=1, \ldots, N_v$. The evolution of each cell in these models is governed by the motion of its vertices, which are typically assumed to obey deterministic equations of motion. It is usual to make the simplifying assumption that the motion of vertices are overdamped (Drasdo, 2000), and inertial terms are small compared with dissipative terms. This leads to first-order dynamics. The evolution of the position r_i of vertex i is determined by:

$$\mu \frac{dr_i}{dt} = F_i(t), \qquad (4)$$

where $F_i(t)$ denotes the total force (except drag) acting on vertex i at time t and μ denotes its drag coefficient. The main difference between models lies in the definition of the force F_i that can be derived from an energy function, E, which includes the different cell-cell interactions. In our model we use a modification of the energy function described in Farhadifar et al. (2007), by including time dependence of the target area term, $A_\alpha^0(t)$. Thus:

$$E = \overbrace{\sum_\alpha \frac{K_\alpha}{2} (A_\alpha - A_\alpha^0(t))^2}^{\text{Elastic energy of cells}} + \overbrace{\sum_{\langle ij \rangle} \Lambda_{ij} l_{ij}}^{\text{Line tension}} + \overbrace{\sum_\alpha \frac{\Gamma_\alpha}{2} L_\alpha^2}^{\text{Global contractility effect}}, \qquad (5)$$

for which $F_i = -\frac{\partial E}{\partial r_i}$.

The first term describes an area elasticity with elasticity coefficients K_α, for which A_α is the area of cell α and $A_\alpha^0(t)$ is the preferred area at time t (the preferred area will be related to the apicobasal nuclear position in this 2D model, Eqn 1). The second term is dependent on the length of cell-cell junctions, representing adhesion/tension energy. It introduces the energy associated with bonds between each cell and its neighbours, where Λ_{ij} is a constant and l_{ij} denotes the length of the junction linking vertices i and j. When Λ_{ij} is negative, cell boundaries tend to expand; when it is positive, the edges tend to shrink. The sum of $\langle ij \rangle$ is over all bonds. The third term describes the contractility of the cell perimeter L_α by a positive coefficient Γ_α, when it is small, contractile forces are small compared with those from area elasticity.

We assume all parameters are the same in each cell or edge, so $K_\alpha=K$, $\Lambda_{ij}=\Lambda$, and $\Gamma_\alpha=\Gamma$. In this case, the final term in Eqn 5 can be expressed as a sum over cell perimeters and combined with the final term to give $\sum_\alpha \frac{\Gamma}{2} (L_\alpha - L_0)^2$, where the target perimeter L_0 is given by $-\Lambda/2\Gamma$. The added constant term is irrelevant, as the dynamics only depend on changes in energy.

Vertex model implementation
The model is implemented with a custom Python code (available in Bitbucket: https://bitbucket.org/Pigueco/vertex_model_python_2.7) using the Euler method to solve the equation of movement for each vertex, Eqn 4. We nondimensionalised in time and space by taking 460 s as a unit of time and using an area of 23 μm^2. The units of force are arbitrary. The tissue is initialized as a hexagonal mesh of 10 by 10 cells, or 15 by 15 cells for simulations with pMN domain. The initial tissue is allowed to evolve for 30 h (biological time) to generate a vertex distribution close to steady state. At this point, the time is reset and the vertex distribution is taken as the starting point for the simulations described in this study.

To accommodate topological transitions in the simulations, we introduced the possibility of T1 transitions. During a T1 transition an edge below 3% of the average edge length of the tissue is eliminated and a new edge of length l_{new} expands perpendicular to the old edge (values given in Table 2). If the rearrangement results in the formation of a two-sided cell, the cell is removed from the epithelium.

Division occurs when the cell is in M-phase ($\tilde{t} > t_{G1} + t_S + t_{G2}$) and the volume of the cell exceeds a critical value, A_c. For a cell to divide, a new edge is introduced by creating two new vertices. The location of the first vertex is chosen as the midpoint of a randomly selected edge of the dividing cell with probability proportional to the edge length. The other vertex is the midpoint of the opposite edge; if the cell has an odd number of sides the second edge is the closer mid edge. The newly generated sister cells then commence the next cell cycle.

In order to define the frequency of cell divisions in the model, we defined the proliferation rate λ as $d/(\tilde{N} \Delta t)$, where d is the number of division events in a small time interval Δt, and $\tilde{N}$ is the average number of cells in the tissue during Δt. For a proliferating tissue in which differentiation does not occur, this estimate of λ is equivalent to the effective rate of tissue growth $k=\ln(N_C(\Delta t)/N_C)/\Delta t$, where Δt is a time interval, N_C is the number of cells in the tissue at the start of the interval and $N_C(\Delta t)$ the number of cells at the end of the interval. To match the experimental data (Kicheva et al., 2014; Table 1), in the simulations we aimed to obtain a proliferation rate of 0.05 h^{-1}. For a proliferating tissue without differentiation $\lambda=\ln(2)/t_T$ where t_T is the total cell cycle time. Thus, $\lambda=0.05$ h^{-1} corresponds to an average cell cycle length of 13 h, which is 10^5 simulation time steps (Tables 1 and 2). In Fig. S6 t_T=13 h is used for the condition with fixed proliferation and varied differentiation. In tissues with high levels of differentiation, however, the proliferation rate is an effective rate because at any one time a fraction of cells present in the tissue will not further divide. Thus, in a tissue with a differentiation rate of 0.1 h^{-1} and effective proliferation rate of 0.05 h^{-1} the cell cycle time of the dividing cells is on average shorter and corresponds to 11.7 h. Note that the estimates of cell cycle duration given in Table 1 are based on fractions of dividing cells from fixed images and are therefore effective measurements. The values of the proliferation rates given in Fig. 4F and Fig. S6 are $ln(2)/t_T$, where t_T is used in simulations to determine the evolution of the target area and the minimum time at which cells can divide. For proliferation rate 0 h^{-1}, t_T is set to 13,000 h. Number of neighbours, cell

11

area and cell perimeter distributions in simulations were compared with output using code from Smith et al. (2012).

Growth of the tissue

We model the neural tube as a torus with two radii, R and H. The torus can grow in both radial directions. The growth in R is resisted by a drag force of magnitude $\mu' \dfrac{dR}{dt}$ per cell. The forces are balanced so drag forces are of the same total magnitude, as the other forces.

Thus, its growth is determined by a balance between the potential forces and drag:

$$\mu' N_c \frac{dR}{dt} = -\frac{\partial E}{\partial R} = -\frac{1}{R} \sum_i x_i \frac{\partial E}{\partial x_i}, \qquad (6)$$

where $x_i = R\theta_i$ is the coordinate that we use for the ith vertex in the dorsoventral direction (Supplementary Materials and Methods, section I).

Equivalently, we calculate growth in the perpendicular direction, H, using the drag coefficient, $2\mu''$.

The tissue aspect ratio (AP/DV) was measured using the whole-tissue AP length and DV length. The AP/DV clone aspect ratio was measured as defined in Kicheva et al. (2014) to enable comparison between experimental data and simulations. In computing the ratio, one nondimensional unit of length is subtracted from the mean AP and mean DV lengths of clones.

Statistical analysis

Statistical analysis details are documented in figure legends and captions. To compare the distributions of cell area, perimeter and number of neighbours of the experimental and simulated data in Fig. 3A and Fig. S2A we quantified the Kolmogorov–Smirnov (K–S) statistic, which measures the difference between distributions. We used mean distributions for the comparison, derived by averaging across 11 images at E11.5 for the experimental data, and 10 runs of the model for the simulated data. We then report the K–S statistic, which represents the largest difference between the mean distributions. Other quantities compared between simulations in Fig. 3A,B and Fig. S3A – cell area standard deviation, cell perimeter standard deviation, DV length of tissue and AP/DV ratio of tissue – were absolute values of the differences between the experimental values and simulation values. The difference between the mean value of 11 images and each of 10 simulation runs was taken and then the mean of these 10 values. In Fig. 3B and Fig. S3A, the values for AP/DV ratio and DV length were then summed.

Competing interests
The authors declare no competing or financial interests.

Author contributions
Conceptualization: P.G., R.P.-C., A.K., J.B., K.M.P.; Methodology: P.G., J.B., K.M.P.; Software: P.G., D.P., K.M.P.; Validation: P.G., M.Z., A.K., K.M.P.; Formal analysis: P.G., R.P.-C., A.K., K.M.P.; Investigation: P.G., R.P.-C., M.Z., A.K., J.B.; Resources: J.B.; Writing - original draft: A.K., J.B., K.M.P.; Writing - review & editing: P.G., R.P.-C., M.Z., A.K., J.B., K.M.P.; Supervision: A.K., J.B., K.M.P.; Project administration: J.B., K.M.P.

Supplementary information
Supplementary information available online at
https://dev.biologists.org/lookup/doi/10.1242/dev.176297.supplemental

References
Aegerter-Wilmsen, T., Smith, A. C., Christen, A. J., Aegerter, C. M., Hafen, E. and Basler, K. (2010). Exploring the effects of mechanical feedback on epithelial topology. *Development* **137**, 499-506. ISSN 0950-1991. doi:10.1242/dev.041731

Aigouy, B., Farhadifar, R., Staple, D. B., Sagner, A., Röper, J.-C., Jülicher, F. and Eaton, S. (2010). Cell flow reorients the axis of planar polarity in the wing epithelium of Drosophila. *Cell* **142**, 773-786. ISSN 1097-4172. doi:10.1016/j.cell.2010.07.042

Alt, S., Ganguly, P. and Salbreux, G. (2017). Vertex models: from cell mechanics to tissue morphogenesis. *Philos. Trans. R. Soc. B Biol. Sci.* **372**, 20150520. doi:10.1098/rstb.2015.0520

Baena-López, L. A., Baonza, A. and García-Bellido, A. (2005). The orientation of cell divisions determines the shape of Drosophila organs. *Curr. Biol.* **15**, 1640-1644. doi:10.1016/j.cub.2005.07.062

Bénazéraf, B., Francois, P., Baker, R. E., Denans, N., Little, C. D. and Pourquié, O. (2010). A random cell motility gradient downstream of FGF controls elongation of an amniote embryo. *Nature* **466**, 248-252. doi:10.1038/nature09151

Bittig, T., Wartlick, O., Kicheva, A., González-Gaitán, M. and Jülicher, F. (2008). Dynamics of anisotropic tissue growth. *New J. Phys.* **10**, 063001. doi:10.1088/1367-2630/10/6/063001

Bosveld, F., Markova, O., Guirao, B., Martin, C., Wang, Z., Pierre, A., Balakireva, M., Gaugue, I., Ainslie, A., Christophorou, N. et al. (2016). Epithelial tricellular junctions act as interphase cell shape sensors to orient mitosis. *Nature* **530**, 495-498. doi:10.1038/nature16970

Bowman, S. K., Neumüller, R. A., Novatchkova, M., Du, Q. and Knoblich, J. A. (2006). The Drosophila NuMA homolog mud regulates spindle orientation in asymmetric cell division. *Dev. Cell* **10**, 731-742. doi:10.1016/j.devcel.2006.05.005

Canela-Xandri, O., Sagués, F., Casademunt, J. and Buceta, J. (2011). Dynamics and mechanical stability of the developing dorsoventral organizer of the wing imaginal disc. *PLoS Comput. Biol.* **7**, e1002153. doi:10.1371/journal.pcbi.1002153

Chiou, K. K., Hufnagel, L. and Shraiman, B. I. (2012). Mechanical stress inference for two dimensional cell arrays. *PLoS Comput. Biol.* **8**, e1002512. doi:10.1371/journal.pcbi.1002512

Classen, A.-K., Anderson, K. I., Marois, E. and Eaton, S. (2005). Hexagonal packing of Drosophila wing epithelial cells by the planar cell polarity pathway. *Dev. Cell* **9**, 805-817. doi:10.1016/j.devcel.2005.10.016

Drasdo, D. (2000). Buckling instabilities of one-layered growing tissues. *Phys. Rev. Lett.* **84**, 4244-4247. doi:10.1103/PhysRevLett.84.4244

Dye, N. A., Popović, M., Spannl, S., Etournay, R., Kainmüller, D., Ghosh, S., Myers, E. W., Jülicher, F. and Eaton, S. (2017). Cell dynamics underlying oriented growth of the *Drosophila* wing imaginal disc. *Development* **144**, 4406-4421. doi:10.1242/dev.155069

Ericson, J., Thor, S., Edlund, T., Jessell, T. and Yamada, T. (1992). Early stages of motor neuron differentiation revealed by expression of homeobox gene islet-1. *Science* **256**, 1555-1560. doi:10.1126/science.1350865

Ericson, J., Morton, S., Kawakami, A., Roelink, H. and Jessell, T. M. (1996). Two critical periods of sonic hedgehog signaling required for the specification of motor neuron identity. *Cell* **87**, 661-673. doi:10.1016/S0092-8674(00)81386-0

Etournay, R., Popović, M., Merkel, M., Nandi, A., Blasse, C., Aigouy, B., Brandl, H., Myers, G., Salbreux, G., Jülicher, F. et al. (2015). Interplay of cell dynamics and epithelial tension during morphogenesis of the Drosophila pupal wing. *eLife* **4**, e07090. doi:10.7554/eLife.07090

Farhadifar, R., Röper, J.-C., Aigouy, B., Eaton, S. and Jülicher, F. (2007). The influence of cell mechanics, cell-cell interactions, and proliferation on epithelial packing. *Curr. Biol.* **17**, 2095-2104. ISSN 0960-9822. doi:10.1016/j.cub.2007.11.049

Finegan, T. M., Na, D., Cammarota, C., Skeeters, A. V., Nádasi, T. J., Dawney, N. S., Fletcher, A. G., Oakes, P. W. and Bergstralh, D. T. (2019). Tissue tension and not interphase cell shape determines cell division orientation in the Drosophila follicular epithelium. *EMBO J.* **38**, e100072. doi:10.15252/embj.2018100072

Fletcher, A. G., Osborne, J. M., Maini, P. K. and Gavaghan, D. J. (2013). Implementing vertex dynamics models of cell populations in biology within a consistent computational framework. *Prog. Biophys. Mol. Biol.* **113**, 299-326. doi:10.1016/j.pbiomolbio.2013.09.003

Fletcher, A. G., Osterfield, M., Baker, R. E. and Shvartsman, S. Y. (2014). Vertex models of epithelial morphogenesis. *Biophys. J.* **106**, 2291-2304. doi:10.1016/j.bpj.2013.11.4498

Gibson, M. C., Patel, A. B., Nagpal, R. and Perrimon, N. (2006). The emergence of geometric order in proliferating metazoan epithelia. *Nature* **442**, 1038-1041. doi:10.1038/nature05014

Gilbert, S. (2014). *Developmental Biology*. Number v. 3 in Developmental Biology. Sinauer Associates, Incorporated Publishers. ISBN 9780878939787.

Gillies, T. E. and Cabernard, C. (2011). Cell division orientation in animals. *Curr. Biol.* **21**, R599-R609. doi:10.1016/j.cub.2011.06.055

Gong, Y., Mo, C. and Fraser, S. E. (2004). Planar cell polarity signalling controls cell division orientation during zebrafish gastrulation. *Nature* **430**, 689-693. doi:10.1038/nature02796

Graustein, W. C. (1931). On the average number of sides of polygons of a net. *Ann. Math.* **32**, 149-153. doi:10.2307/1968421

Guirao, B., Rigaud, S. U., Bosveld, F., Bailles, A., López-Gay, J., Ishihara, S., Sugimura, K., Graner, F. and Bellaïche, Y. (2015). Unified quantitative characterization of epithelial tissue development. *eLife* **4**, e08519. doi:10.7554/eLife.08519

Hilgenfeldt, S., Erisken, S. and Carthew, R. W. (2008). Physical modeling of cell geometric order in an epithelial tissue. *Proc. Natl Acad. Sci. USA* **105**, 907-911. doi:10.1073/pnas.0711077105

Honda, H. and Nagai, T. (2015). Cell models lead to understanding of multi-cellular morphogenesis consisting of successive self-construction of cells. *J. Biochem.* **157**, 129-136. doi:10.1093/jb/mvu088

Kafer, J., Hayashi, T., Maree, A. F. M., Carthew, R. W. and Graner, F. (2007). Cell adhesion and cortex contractility determine cell patterning in the *Drosophila* retina. *Proc. Natl Acad. Sci. USA* **104**, 18549-18554. doi:10.1073/pnas.0704235104

Kicheva, A., Bollenbach, T., Ribeiro, A., Valle, H. P., Lovell-Badge, R., Episkopou, V. and Briscoe, J. (2014). Coordination of progenitor specification and growth in mouse and chick spinal cord. *Science* **345**, 1254927. ISSN 0036-8075. doi:10.1126/science.1254927

Kokic, M., Iannini, A., Villa-Fombuena, G., Casares, F. and Iber, D. (2019). Minimisation of surface energy drives apical epithelial organisation and gives rise to Lewis' law. *bioRxiv* 590729. doi:10.1101/590729

Konno, D., Shioi, G., Shitamukai, A., Mori, A., Kiyonari, H., Miyata, T. and Matsuzaki, F. (2008). Neuroepithelial progenitors undergo LGN-dependent planar divisions to maintain self-renewability during mammalian neurogenesis. *Nat. Cell Biol.* **10**, 93-101. doi:10.1038/ncb1673

Kursawe, J., Brodskiy, P. A., Zartman, J. J., Baker, R. E. and Fletcher, A. G. (2015). Capabilities and limitations of tissue size control through passive mechanical forces. *PLoS Comput. Biol.* **11**, 1-26. ISSN 15537358. doi:10.1371/journal.pcbi.1004679

Kursawe, J., Baker, R. E. and Fletcher, A. G. (2018). Approximate bayesian computation reveals the importance of repeated measurements for parameterising cell-based models of growing tissues. *J. Theor. Biol.* **443**, 66-81. doi:10.1016/j.jtbi.2018.01.020

Landsberg, K. P., Farhadifar, R., Ranft, J., Umetsu, D., Widmann, T. J., Bittig, T., Said, A., Jülicher, F. and Dahmann, C. (2009). Increased cell bond tension governs cell sorting at the Drosophila anteroposterior compartment boundary. *Curr. Biol.* **19**, 1950-1955. ISSN 0960-9822. doi:10.1016/j.cub.2009.10.021

Lecuit, T. and Lenne, P.-F. (2007). Cell surface mechanics and the control of cell shape, tissue patterns and morphogenesis. *Nat. Rev. Mol. Cell Biol.* **8**, 633-644. doi:10.1038/nrm2222

LeGoff, L., Rouault, H. and Lecuit, T. (2013). A global pattern of mechanical stress polarizes cell divisions and cell shape in the growing Drosophila wing disc. *Development* **140**, 4051-4059. doi:10.1242/dev.090878

Li, Y., Naveed, H., Kachalo, S., Xu, L. X. and Liang, J. (2014). Mechanisms of regulating tissue elongation in Drosophila wing: Impact of oriented cell divisions, oriented mechanical forces, and reduced cell size. *PLoS ONE* **9**, e86725. doi:10.1371/journal.pone.0086725

Magno, R., Grieneisen, V. A. and Marée, A. F. M. (2015). The biophysical nature of cells: potential cell behaviours revealed by analytical and computational studies of cell surface mechanics. *BMC Biophysics* **8**, 8. ISSN 2046-1682. doi:10.1186/s13628-015-0022-x

Mao, Y., Tournier, A. L., Bates, P. A., Gale, J. E., Tapon, N. and Thompson, B. J. (2011). Planar polarization of the atypical myosin dachs orients cell divisions in Drosophila. *Genes Dev.* **25**, 131-136. doi:10.1101/gad.610511

Mao, Y., Tournier, A. L., Hoppe, A., Kester, L., Thompson, B. J. and Tapon, N. (2013). Differential proliferation rates generate patterns of mechanical tension that orient tissue growth. *EMBO J.* **32**, 2790-2803. doi:10.1038/emboj.2013.197

Merkel, M. and Manning, M. L. (2017). Using cell deformation and motion to predict forces and collective behavior in morphogenesis. *Semin. Cell Dev. Biol.* **67**, 161-169. doi:10.1016/j.semcdb.2016.07.029

Mongera, A., Rowghanian, P., Gustafson, H. J., Shelton, E., Kealhofer, D. A., Carn, E. K., Serwane, F., Lucio, A. A., Giammona, J. and Campàs, O. (2018). A fluid-to-solid jamming transition underlies vertebrate body axis elongation. *Nature* **561**, 401-405. doi:10.1038/s41586-018-0479-2

Morin, X., Jaouen, F. and Durbec, P. (2007). Control of planar divisions by the g-protein regulator LGN maintains progenitors in the chick neuroepithelium. *Nat. Neurosci.* **10**, 1440-1448. doi:10.1038/nn1984

Nagai, T. and Honda, H. (2001). A dynamic cell model for the formation of epithelial tissues. *Philos. Mag. B* **81**, 699-719. doi:10.1080/13642810108205772

Ranft, J., Basan, M., Elgeti, J., Joanny, J.-F., Prost, J. and Jülicher, F. (2010). Fluidization of tissues by cell division and apoptosis. *Proc. Natl Acad. Sci. USA* **107**, 20863-20868. doi:10.1073/pnas.1011086107

Ray, R. P., Matamoro-Vidal, A., Ribeiro, P. S., Tapon, N., Houle, D., Salazar-Ciudad, I. and Thompson, B. J. (2015). Patterned anchorage to the apical extracellular matrix defines tissue shape in the developing appendages of Drosophila. *Dev. Cell* **34**, 310-322. doi:10.1016/j.devcel.2015.06.019

Rousso, D. L., Pearson, C. A., Gaber, Z. B., Miquelajauregui, A., Li, S., Portera-Cailliau, C., Morrisey, E. E. and Novitch, B. G. (2012). Foxp-mediated suppression of n-cadherin regulates neuroepithelial character and progenitor maintenance in the CNS. *Neuron* **74**, 314-330. doi:10.1016/j.neuron.2012.02.024

Sagner, A., Gaber, Z. B., Delile, J., Kong, J. H., Rousso, D. L., Pearson, C. A., Weicksel, S. E., Melchionda, M., Gharavy, S. N. M., Briscoe, J. et al. (2018). Olig2 and hes regulatory dynamics during motor neuron differentiation revealed by single cell transcriptomics. *PLoS Biol.* **16**, e2003127. doi:10.1371/journal.pbio.2003127

Salbreux, G., Barthel, L. K., Raymond, P. A. and Lubensky, D. K. (2012). Coupling mechanical deformations and planar cell polarity to create regular patterns in the zebrafish retina. *PLoS Comput. Biol.* **8**, e1002618. doi:10.1371/journal.pcbi.1002618

Sauer, F. C. (1935). Mitosis in the neural tube. *J. Comp. Neurol.* **62**, 377-405. doi:10.1002/cne.900620207

Seldin, L. and Macara, I. (2017). Epithelial spindle orientation diversities and uncertainties: recent developments and lingering questions. *F1000 Res.* **6**, 984. doi:10.12688/f1000research.11370.1

Shraiman, B. I. (2005). Mechanical feedback as a possible regulator of tissue growth. *Proc. Natl Acad. Sci. USA* **102**, 3318-3323. ISSN 0027-8424. doi:10.1073/pnas.0404782102

Smith, A. M., Baker, R. E., Kay, D. and Maini, P. K. (2012). Incorporating chemical signalling factors into cell-based models of growing epithelial tissues. *J. Math. Biol.* **65**, 441-463. doi:10.1007/s00285-011-0464-y

Strzyz, P., Matejcic, M. and Norden, C. (2016). Heterogeneity, cell biology and tissue mechanics of pseudostratified epithelia: Coordination of cell divisions and growth in tightly packed tissues. *Int. Rev. Cell Mol. Biol.* **325**, 89-118. doi:10.1016/bs.ircmb.2016.02.004

Sugimura, K. and Ishihara, S. (2013). The mechanical anisotropy in a tissue promotes ordering in hexagonal cell packing. *Development* **140**, 4091-4101. doi:10.1242/dev.094060

Trichas, G., Smith, A. M., White, N., Wilkins, V., Watanabe, T., Moore, A., Joyce, B., Sugnaseelan, J., Rodriguez, T. A., Kay, D. et al. (2012). Multi-cellular rosettes in the mouse visceral endoderm facilitate the ordered migration of anterior visceral endoderm cells. *PLoS Biol.* **10**, e1001256. doi:10.1371/journal.pbio.1001256

Wartlick, O., Mumcu, P., Kicheva, A., Bittig, T., Seum, C., Jülicher, F. and Gonzalez-Gaitan, M. (2011). Dynamics of dpp signaling and proliferation control. *Science* **331**, 1154-1159. doi:10.1126/science.1200037

Wyatt, T. P. J., Harris, A. R., Lam, M., Cheng, Q., Bellis, J., Dimitracopoulos, A., Kabla, A. J., Charras, G. T. and Baum, B. (2015). Emergence of homeostatic epithelial packing and stress dissipation through divisions oriented along the long cell axis. *Proc. Natl Acad. Sci. USA* **112**, 5726-5731. doi:10.1073/pnas.1420585112
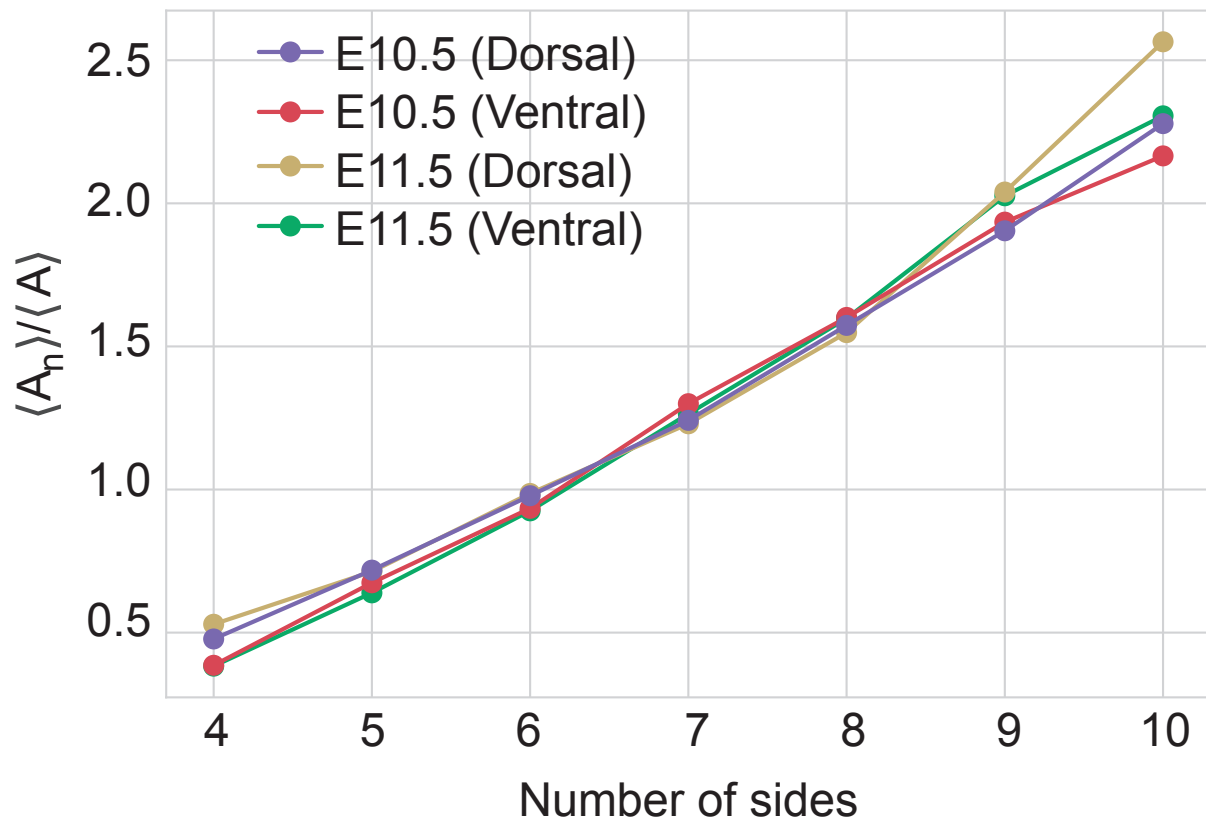
Fig. S1. Average area of different polygon classes Mean areas of different polygon classes normalised to the average area of cells, $\langle A_n \rangle / \langle A \rangle$, in experimental data from the ventral and dorsal domains at mouse neural tube stage E10.5 and E11.5.
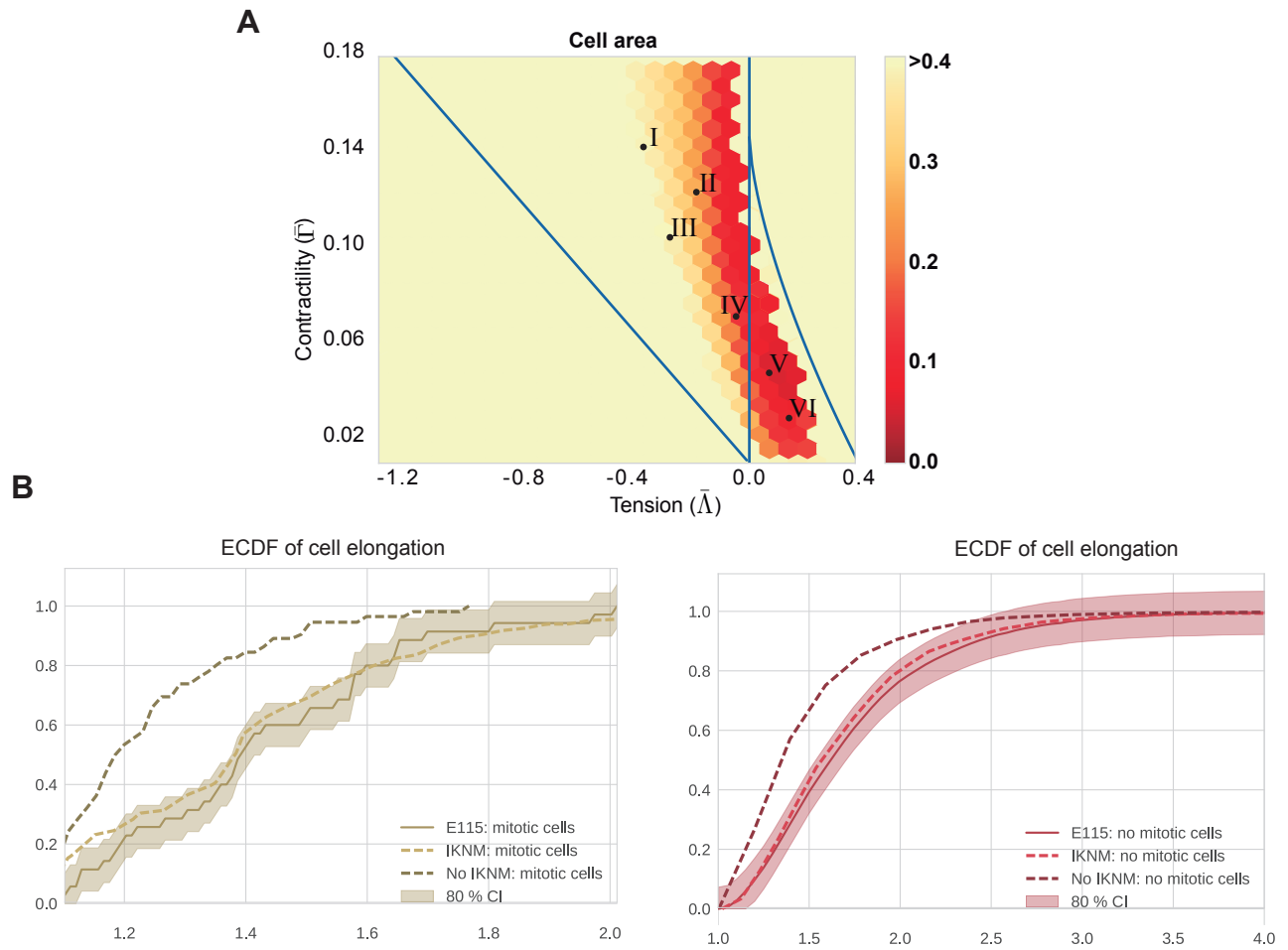
Fig. S2. Simulations without IKNM match experimental data less well A) Map of the average of maximum distance between the experimental and simulated empirical cumulative distribution function of cell area distribution for a model without IKNM (constant target area). Experimental data corresponds to E11.5 embryos and simulations correspond to 10 simulations per point in the parameter space. Roman numeral marked points indicate the mechanical parameters selected, $(\bar{\Lambda}, \bar{\Gamma})$ in Fig. 3A. B) Empirical cumulative distribution function (ECDF) of cell elongation in simulations with and without IKNM using mechanical parameter V in Fig. 3A compared to E11.5 experimental data of mitotic and non-mitotic cells (left and right respectively).
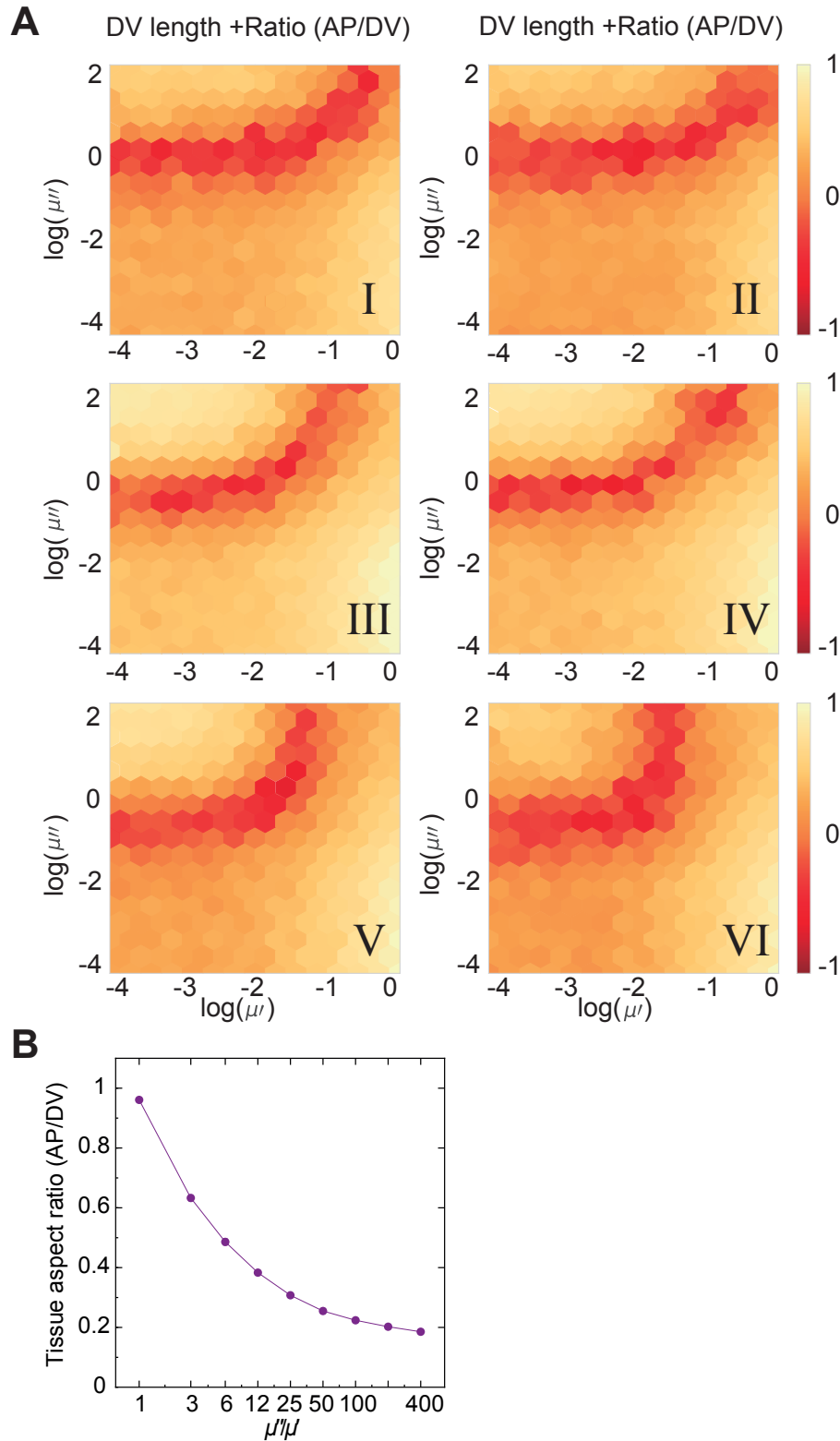
Fig. S3. Determining drag coefficients that generate anisotropic growth in simulations A) Heatmap indicating the difference between simulation and experimental tissues for different values of the drag coefficients μ' and μ''. The absolute value of the difference in the change in DV length of the tissue over 48h plus the absolute value of the difference in the final tissue aspect ratio (AP/DV) between simulations and experimental data was taken and then this quantity was averaged over 10 simulations. Colour map shows the average difference (log scale) from 10 different simulations per point with the experimental data from E11.5 embryos. Other parameters are indicated in Table 2. Roman numerals indicate mechanical parameters used ($\bar{\Lambda}$, $\bar{\Gamma}$) in Fig. 3A. B) The AP/DV aspect ratio of simulated tissues at the end of the simulation (72h) for a range of μ''/μ' ratios. $\mu'' = 1$ is held constant and μ' is varied from 0.0025 to 1. The proliferation rate is $0.05h^{-1}$ and there is no differentiation. Parameter regime V is used. The reported errors are SE.
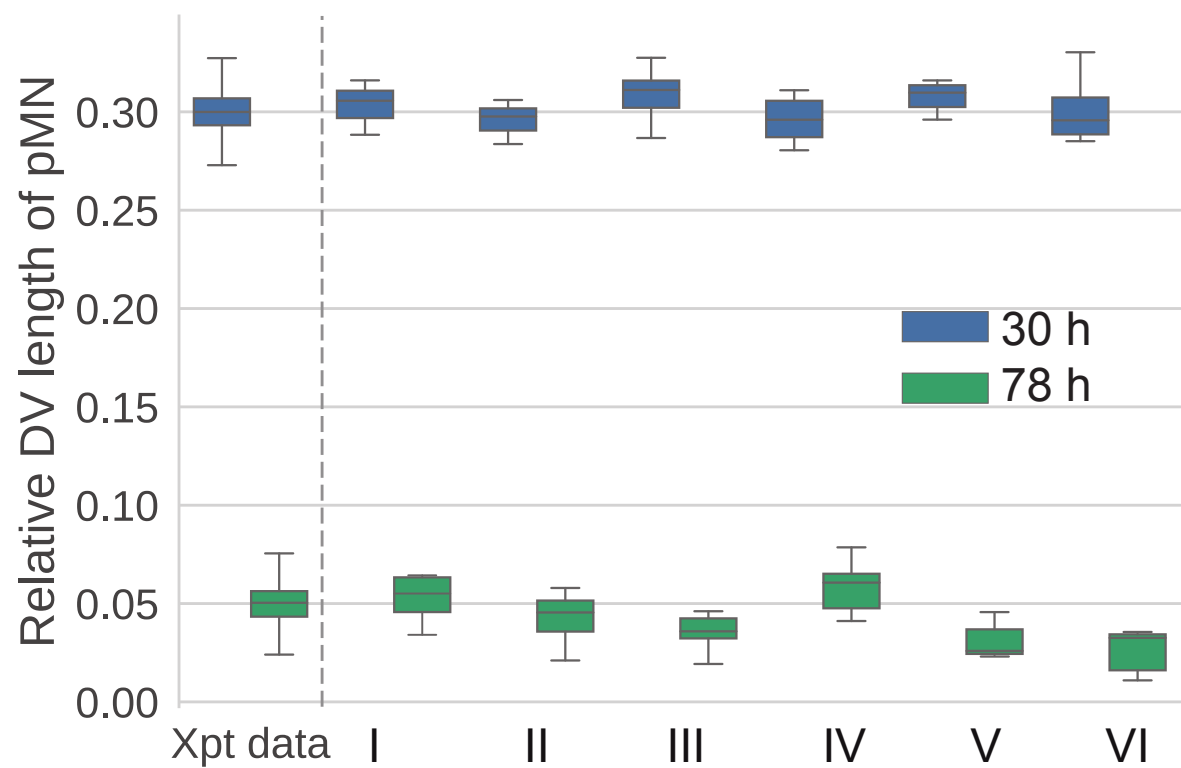
Fig. S4. The effect of introducing differentiation on DV length of the pMN domain DV length of the pMN domain relative to the total DV length of the tissue at the point pMN is introduced to simulations (blue) and after 48 hours (green). Differentiation rate in pMN domain $0.1h^{-1}$. Other parameters are indicated in Table 2. These time points correspond to experimental samples (Xpt data) from E9.5 and E11.5 mouse embryos, respectively. The DV length at these developmental stages was measured in (Kicheva et al. (2014)).
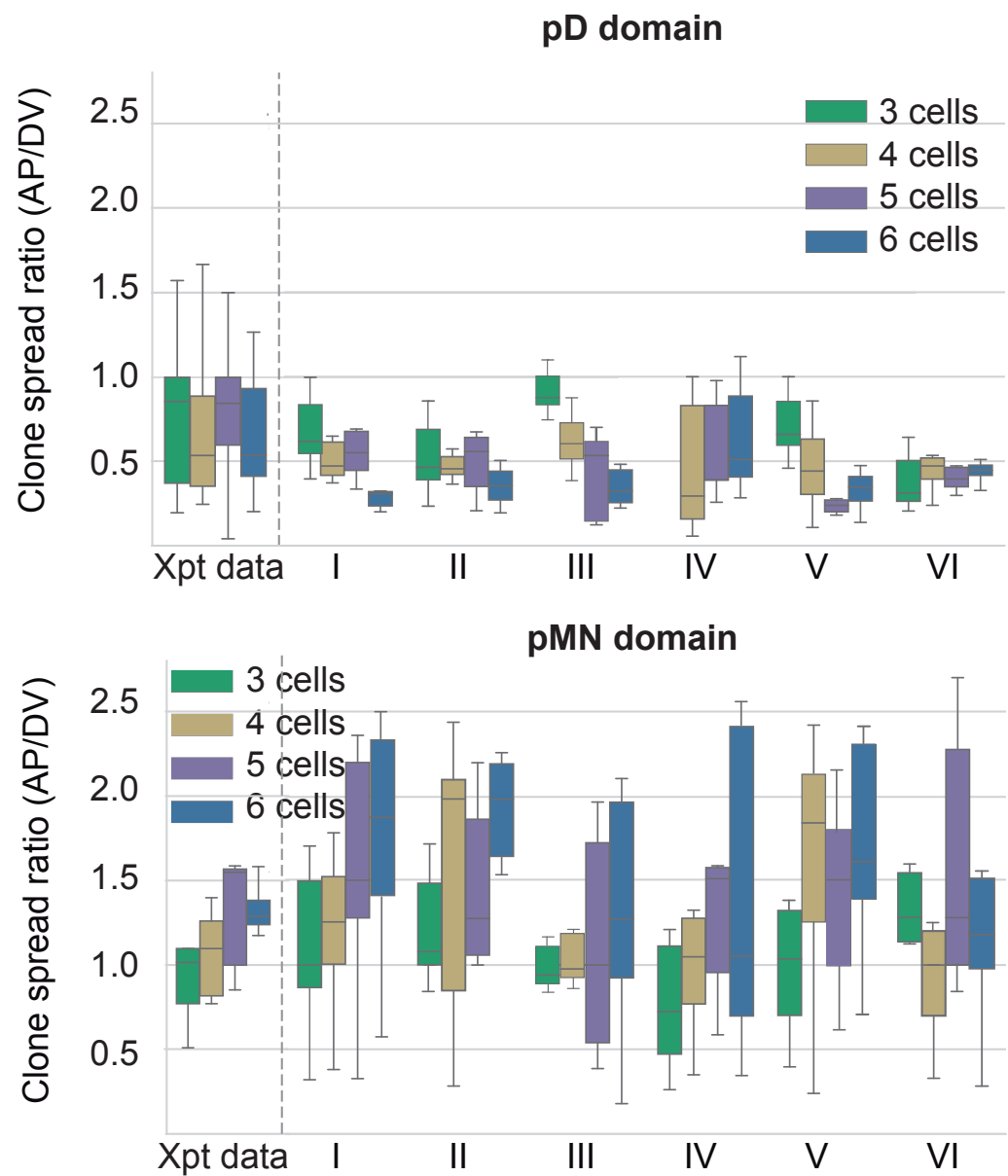
Fig. S5. Shape of clones of different size in the pD and pMN domain The AP/DV aspect ratio for clones containing the indicated number of cells per clone (3 green, 4 yellow, 5 purple, 6 blue) in the pD and pMN domains. Experimental samples (Xpt data) are compared to the result of 12 simulations per mechanical parameter set $(\bar{\Lambda}, \bar{\Gamma})$ from Fig. 3A. Differentiation rate in pMN is $0.1h^{-1}$. Other parameters are indicated in Table 2.
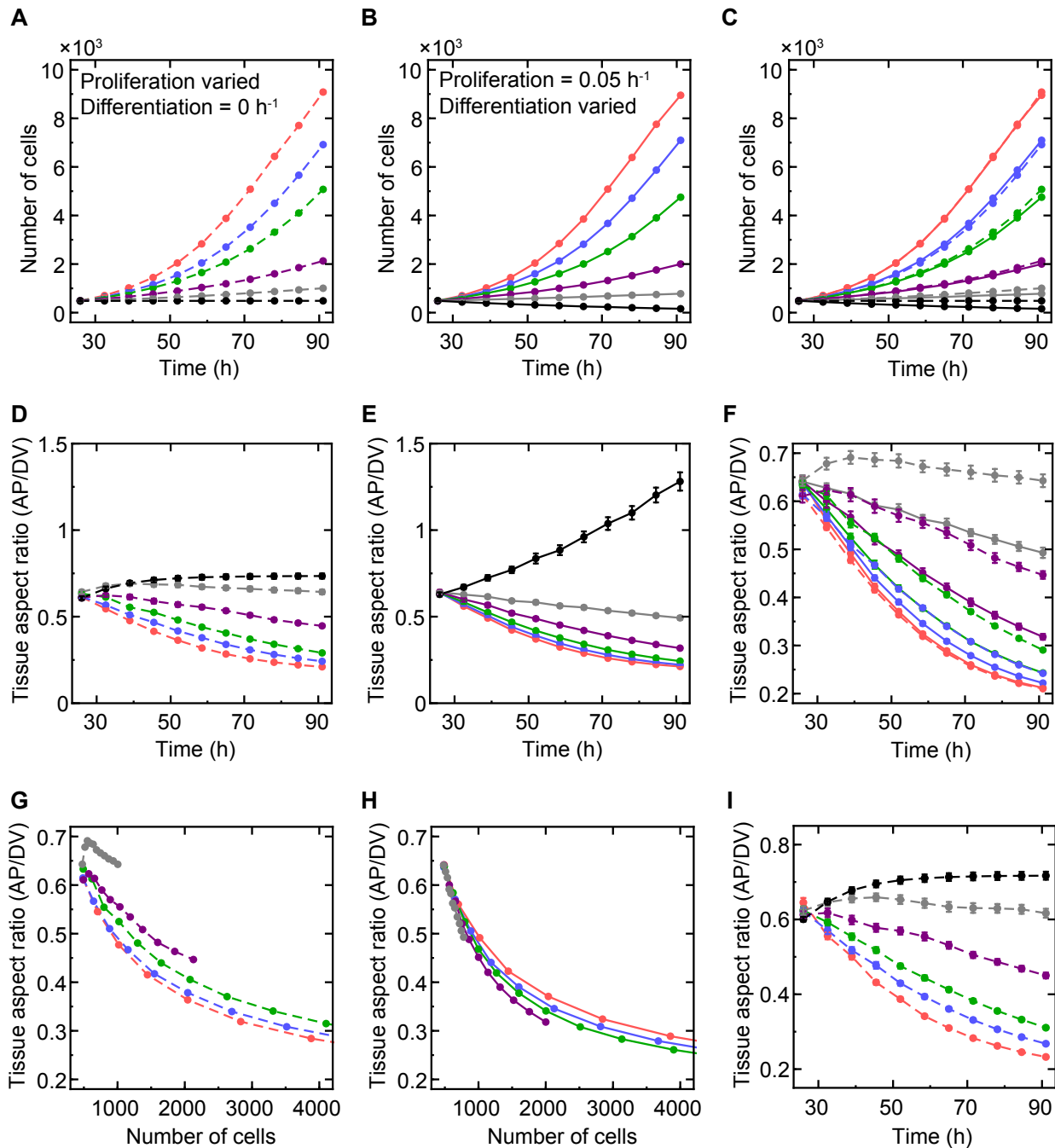
Fig. S6. Effect of proliferation and differentiation rate on the size and shape of simulated neuroepithelial tissue A) Number of cells in simulated tissues as a function of time for different proliferation rates and no differentiation. The proliferation rates from top to bottom: $0.05h^{-1}$ (red), $0.04h^{-1}$ (blue), $0.03h^{-1}$ (green), $0.02h^{-1}$ (purple), $0.01h^{-1}$ (grey), $0h^{-1}$ (black). In A-I: the simulation starts with an initial period of ($t < 26h$) during which the proliferation rate is $0.05h^{-1}$ and there is no differentiation. Afterwards proliferation or differentiation is altered as indicated. In A-H parameter regime V is used. B) The number of cells as a function of time for different differentiation rates and fixed proliferation rate = $0.05h^{-1}$. The differentiation rate is $0h^{-1}$ (red), $0.01h^{-1}$ (blue), $0.02h^{-1}$ (green), $0.035h^{-1}$ (purple), $0.05h^{-1}$ (grey), $0.075h^{-1}$ (black). The parameters were chosen so that the net growth rate in B is similar to that in A for curves of the same colour (except black). C) Overlaid data from A and B. D) Aspect ratio of the tissue AP to DV extension for varied proliferation and no differentiation (same as main Fig. 4F, parameters as in A). E) As D but for varied differentiation and fixed proliferation (parameters as in B). F) Overlaid data from D and E. Only simulations with positive net growth rate are plotted (no black trajectories). G, H) The tissue aspect ratio (AP/DV) from D and E as a function of cell number. Only conditions with positive growth rate are shown. I) The tissue aspect ratio (AP/DV) for varied proliferation and no differentiation in parameter regime VI. The proliferation rates and colour convention as in (A). Data A-I was averaged over 12 independent simulations for each condition. The reported errors are SEM. If error bars are not visible the SEM was very small ($<2\%$).
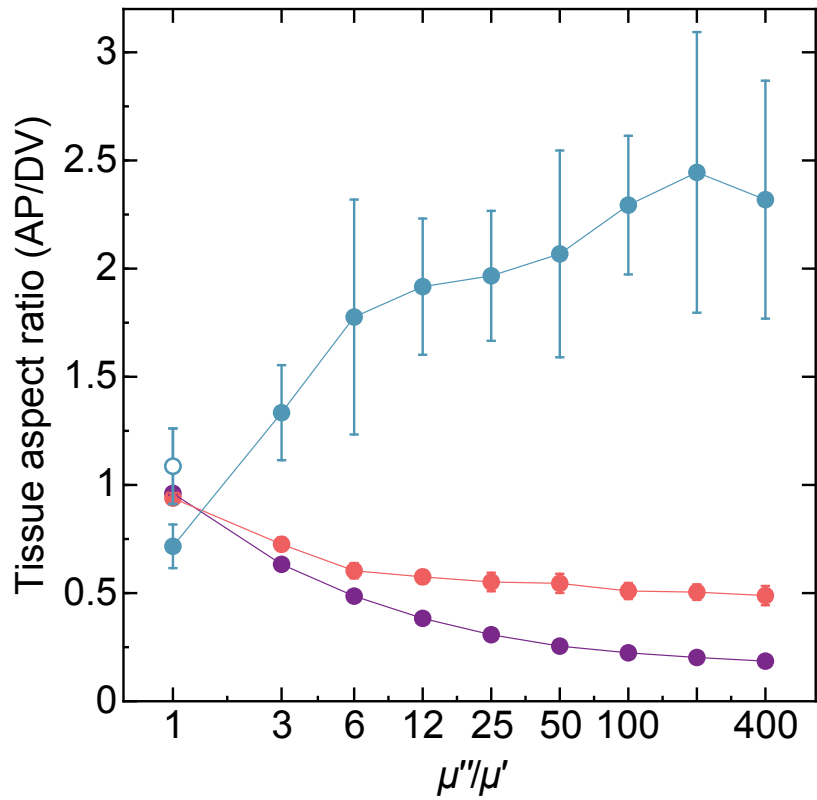
Fig. S7. Influence of the ratio of the AP/DV drag coefficients on the shape of tissue with different rates of differentiation Increasing the differentiation rate increases the AP/DV aspect ratio of simulated tissues for all μ''/μ' ratios larger than 1. The AP/DV aspect ratio at the end of the simulation (72h) is reported. The simulation starts with an initial period of ($t < 26h$) during which the proliferation rate is $0.05h^{-1}$ and there is no differentiation. Afterwards differentiation is altered: $0h^{-1}$ (purple, same as in Fig. S.3B), $0.05h^{-1}$ (red), $0.1h^{-1}$ (solid light blue). The indicated μ''/μ' ratio is fixed from the start. The parameter regime V is used. In the case μ''/μ'=1, the final AP/DV aspect ratio is <1. This is because the tissue is initialized with hexagonal mesh of 10 by 10 cells (honeycomb pattern) that has the AP/DV ratio = $\sqrt{3}/2 \approx 0.87$. If the tissue is initialized with hexagonal mesh of 10 cells in DV direction and 12 cells in AP direction (initial AP/DV ratio ≈ 1.04), then the end result is also isotropic as expected (empty light blue dot). The reported errors are SE.

Simulation data

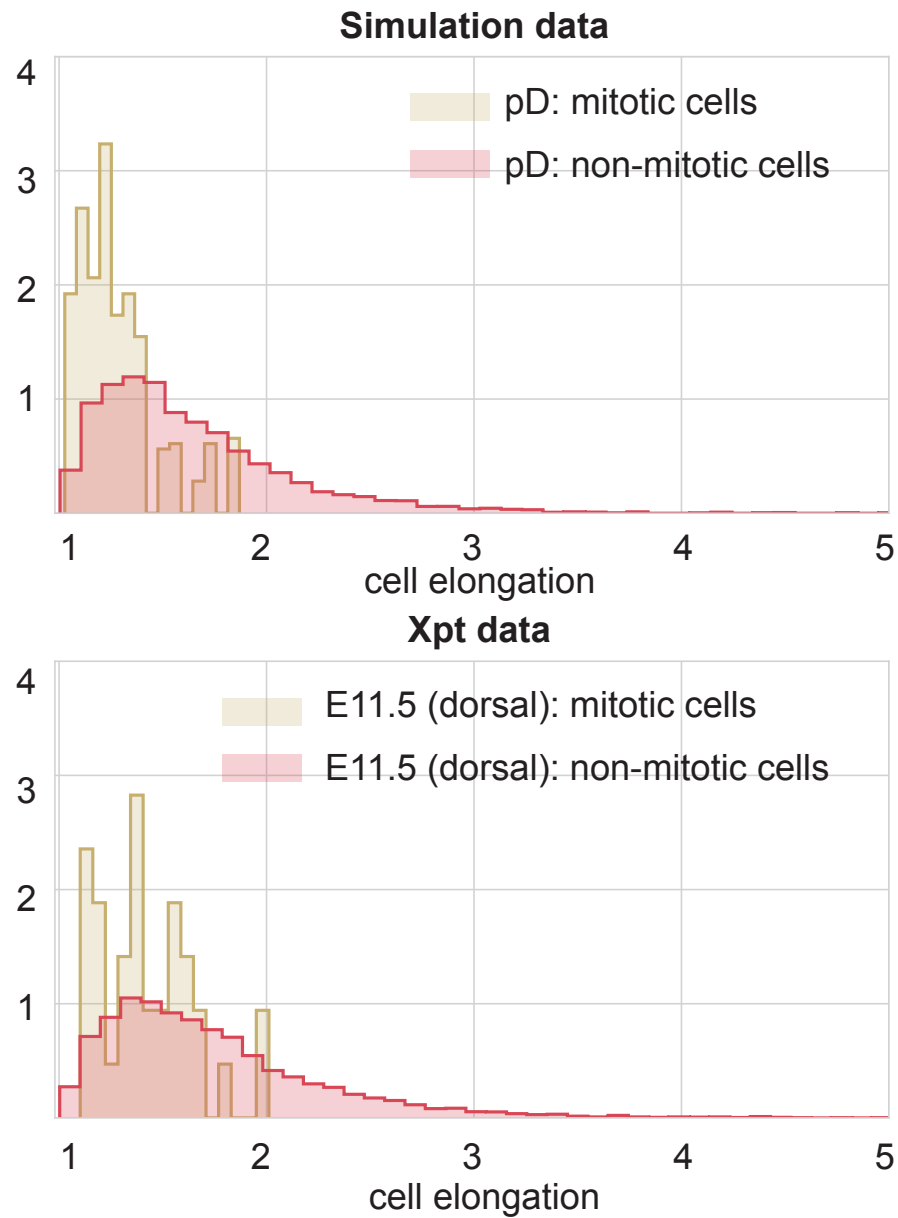cell elongation

Xpt data

cell elongation

Fig. S8. Cell elongation in simulated tissue and experimental data Histogram of cell elongation in cells close to mitosis (brown) and non-mitotic (red) cells in simulations and experimental data in the dorsal domain. In the experimental data, the 2.5% of cells with largest area were considered mitotic. For the simulations, parameter regime V was used.
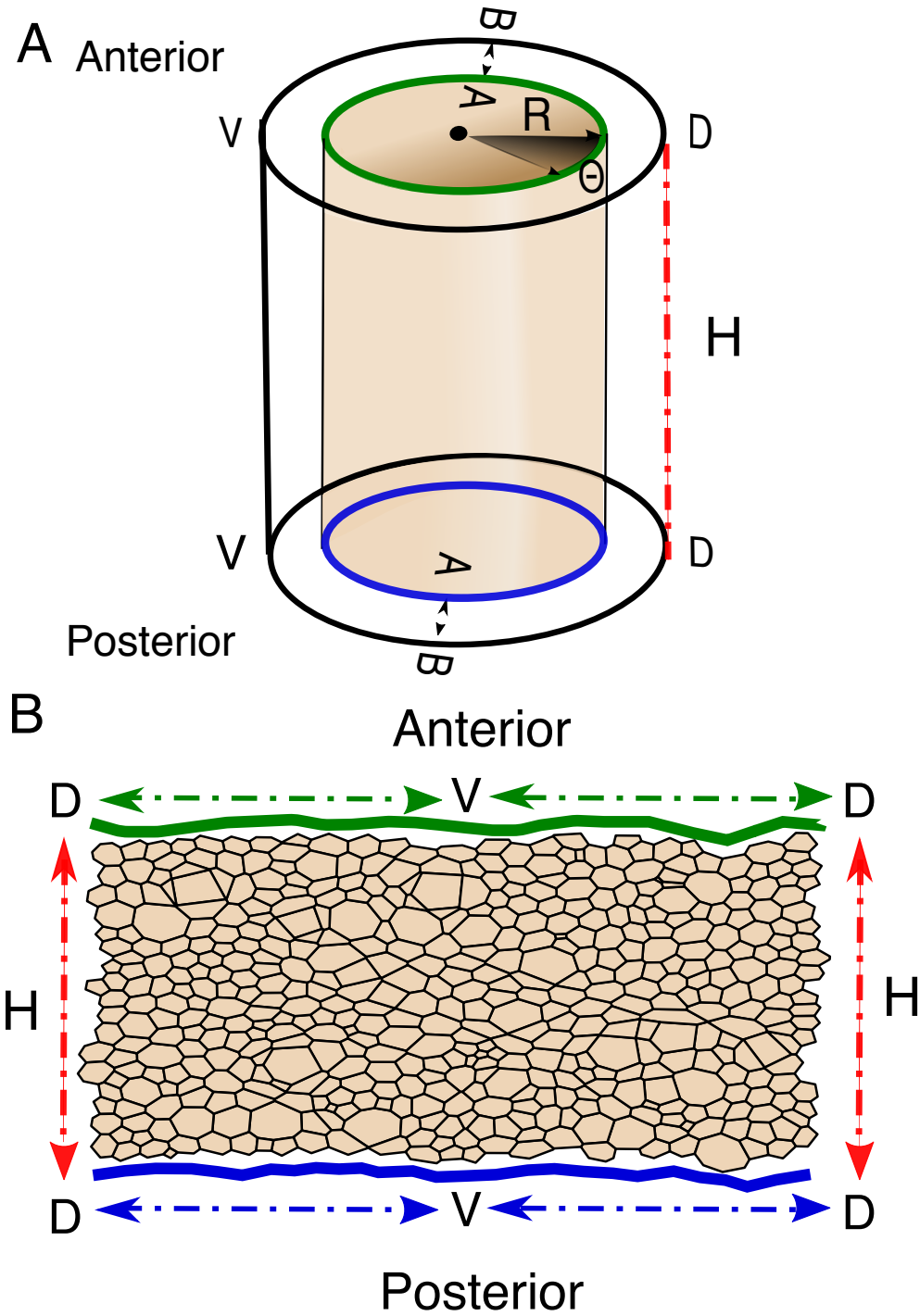
Fig. S9. Cylindrical representation of the neural tube A) Cylindrical representation where R is the radius, θ is the angle and H is height of the cylinder and the z-axis is along this length. B) Polygon representation of the apical junctional network.
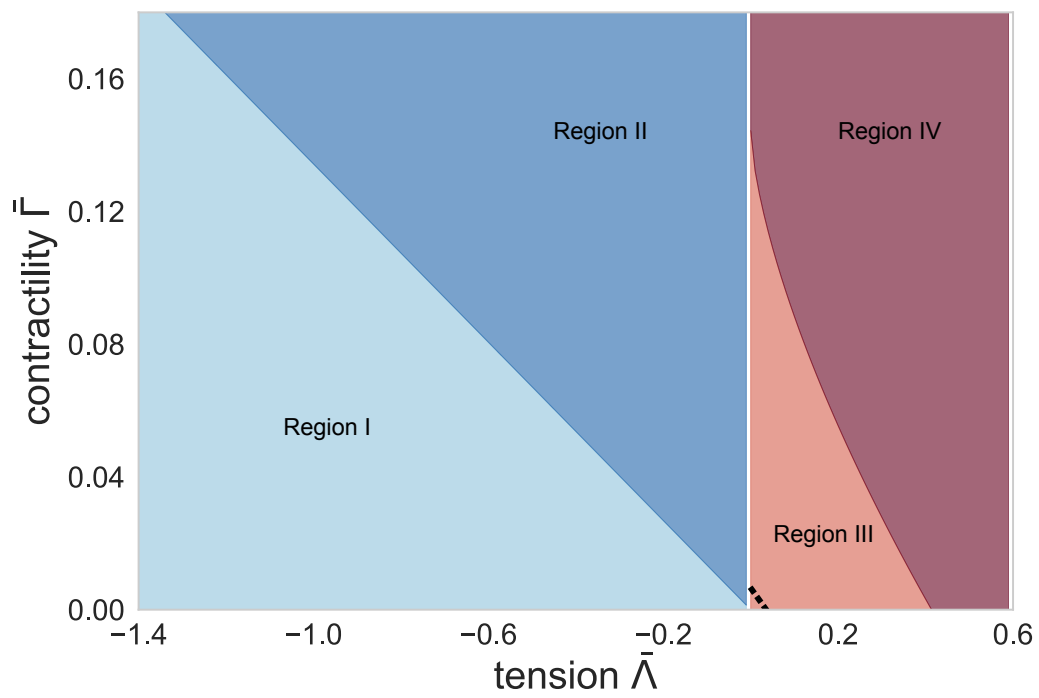
Fig. S10. **Phase diagram** Phase diagram for the biophysical parameter space for hexagonal cells in terms of $\bar{\Lambda}$ and $\bar{\Gamma}$.

Supplementary Materials and Methods: Neuronal differentiation influences progenitor arrangement in the vertebrate neuroepithelium

I. CYLINDRICAL REPRESENTATION

The domain of the vertex model is a cylinder, the radius, R, and height, H, of which can change in time. A natural set of coordinates for the vertex i within the cylinder are $(\theta_i, \tilde{z}_i)$, where θ_i are cylindrical polar angles and $\tilde{z}_i = z_i/H$, where z_i is the coordinate in the direction along the length of the cylinder, see Fig. S9. Note that in simulations we actually impose periodic boundary conditions also in the direction along the length of the cylinder. The movement of vertices is determined by an energy function, E.

We assume overdamped movement, with the drag coefficient for vertices within the cylinder (whilst the cylinder size is fixed) being μ. Therefore:

$$\mu R \frac{d\theta_i}{dt} = -\frac{1}{R}\frac{\partial E}{\partial \theta_i}, \qquad \text{(SM.1)}$$

$$\mu H \frac{d\tilde{z}_i}{dt} = -\frac{1}{H}\frac{\partial E}{\partial \tilde{z}_i}. \qquad \text{(SM.2)}$$

In addition the cylinder itself can grow. We assume that cells (whose average areas are constant) experience some drag proportional to their speed, both radial and tangential (frictional) as the outside surface of the cylinder expands. Radially the speed of each cell is $\frac{dR}{dt}$ and along the length of the cylinder, the velocities are on average $\frac{1}{2}\frac{dH}{dt}$ relative to a fixed point at one end of the cylinder [1]. Let us define the relevant drag coefficients to be μ' radially and $2\mu''$ along the length of the cylinder. The equation for the radius and the height are determined by the balance between the radial component (the height component) of the potential forces and the accumulated drag on all of the cells:

$$\mu' N_c \frac{dR}{dt} = -\frac{\partial E}{\partial R}, \mu'' N_c \frac{dH}{dt} = -\frac{\partial E}{\partial H}, \qquad \text{(SM.3)}$$

where N_c is the number of cells. We note that the three drag coefficients μ, μ' and $2\mu''$ are likely to be different. We also note when a cell is added its energy is added to E.

The coordinates that we actually use in the vertex model code are given by (x_i, z_i), where $x_i = R\theta_i$ and $z_i = H\tilde{z}_i$, which are effectively rectangular coordinates in a folded out cylinder. The equation for the radius, thus becomes:

$$N_c\mu'\frac{dR}{dt} = -\sum_i \frac{\partial E}{\partial x_i}\frac{\partial x_i}{\partial R} = -\frac{1}{R}\sum_i x_i \frac{\partial E}{\partial x_i}. \qquad \text{(SM.4)}$$

_____

[1] The magnitude of the overall force is the same if we consider the middle of the cylinder as being stationary.

Therefore

$$\frac{dx_i}{dt} = -\frac{1}{\mu}\frac{\partial E}{\partial x_i} - \frac{1}{\mu'}\frac{x_i}{N_c R^2}\sum_j x_j \frac{\partial E}{\partial x_j}. \qquad \text{(SM.5)}$$

Similarly,

$$\frac{dz_i}{dt} = -\frac{1}{\mu}\frac{\partial E}{\partial z_i} - \frac{1}{\mu''}\frac{z_i}{N_c H^2}\sum_j z_j \frac{\partial E}{\partial z_j}. \qquad \text{(SM.6)}$$

In the code, we update x_i and z_i first according to equation (SM.1) and (SM.2), (i.e. in time step Δt we add $R\Delta\theta_i$ and $H\Delta\tilde{z}_i$), then we multiply by a factor $\frac{R+\Delta R}{R}$ and $\frac{H+\Delta H}{H}$ respectively, where we call $\frac{\Delta R}{R}$ and $\frac{\Delta H}{H}$ "expansion" and these are given by $-\frac{\Delta t}{N_c\mu'R^2}\sum_j x_j \frac{\partial E}{\partial x_j}$ and $-\frac{\Delta t}{N_c\mu''H^2}\sum_j z_j \frac{\partial E}{\partial z_j}$.

II. BIOPHYSICAL PARAMETER SPACE

We study the effect of the biophysical parameters on the cell dynamics. The energy (Eq. 4) is determined by the vertex positions and parameters K, Λ, and Γ. Magno et al. [2015] find parameter regions that yield different behaviours depending on the mechanical parameters.

The energy E for an individual cell is given by:

$$E = \frac{K}{2}(A - A^0)^2 + \frac{\Lambda}{2}L + \frac{\Gamma}{2}L^2. \qquad \text{(SM.7)}$$

The interfacial tension γ and pressure Π are given by

$$\gamma = \frac{\partial E}{\partial L} = \frac{\Lambda}{2} + \Gamma L, \qquad \text{(SM.8)}$$

$$\Pi = -\frac{\partial E}{\partial A} = -K(A - A^0). \qquad \text{(SM.9)}$$

A reduction in cell perimeter reduces the energy and is therefore favoured. This favours cells that take a regular shape, hence we require the interfacial tension to be positive,

$$\gamma = \frac{\Lambda}{2} + \Gamma L > 0. \qquad \text{(SM.10)}$$

This should be true for the equilibrium cell size.

Suppose a cell has a fixed shape and denote the square root of its area by l and its shape index by $s = L/\sqrt{A}$ where L and A are the perimeter and the area cell. The equilibrium size is determined by setting $\frac{\partial E}{\partial l} = 0$:

$$\frac{\partial E}{\partial l} = \gamma \frac{dL}{dl} - \Pi \frac{dA}{dl} = 0, \qquad \text{(SM.11)}$$

thus at equilibrium $\gamma s = 2\Pi l$, and therefore

$$2Kl^3 = -\frac{\Lambda}{2}s + (2KA^0 - \Gamma s^2)l. \qquad \text{(SM.12)}$$

We note that when $l = 0$, $\frac{\partial E}{\partial l} = \Lambda s$, so the state $l = 0$ is stable if and only if $\Lambda > 0$. Eq. SM.12 has a single positive solution corresponding to an energy minimum if $\Lambda < 0$ (meaning cells converge to a single equilibrium area). If $\Lambda > 0$, Eq. SM.12 can either have zero positive solutions (in which case all cells collapse to zero area) or two positive solutions. In the latter case, the larger positive solution will correspond to an energy minimum and the small positive solution to an energy maximum. Thus cells with area greater than the unstable value will expand their area towards a fixed positive value, while the area of small cells will collapse to zero.

We note that the condition for the state $l = 0$ to be unstable is independent of the target area. In our model, the target area varies slowly compared to the movement of vertices and thus we expect this property to hold for the same parameter values in the model with varying target area too. The condition for regularly shaped cells does depend on the target area, since when interfacial tension is zero, the minimum energy will be attained when cell area is equal to target area. With other parameters fixed, as the target area increases, the interfacial tension will also increase and so cells will tend to be more regular. Thus it is possible that small cells will be irregularly shaped, but larger ones will be regularly shaped. This is because for small cells the adhesive force will dominate the force from the actomyosin ring, whereas for larger cells, the opposite will be true.

The final condition that we need to determine is the condition for there to be two positive steady states instead of zero when $\Lambda > 0$. There are two positive states if and only if

$$A^0 > \frac{\Gamma s^2}{2K} + \frac{3}{4}\left(\frac{\Lambda s}{K}\right)^{2/3}. \qquad (SM.13)$$

This condition depends on our variable target area. What really matters, however, is whether cells are likely to grow at any size that they attain (i.e. it does not matter if we are in the region with two stable areas if the cells are so small when they are born that they shrink to zero). A necessary condition for cells to shrink from their size at birth is that $\left.\frac{\partial E}{\partial l}\right|_{l=\sqrt{A_c/2}} < 0$ with the target area given by its value at the start of the cell cycle. A sufficient condition is that $\left.\frac{\partial E}{\partial l}\right|_{l=\sqrt{A_c/2}} < 0$ with the target area given by its minimal value. Now

$$\left.\frac{\partial E}{\partial l}\right|_{l=\sqrt{A_c/2}} = \frac{\Lambda}{2}s + \Gamma s^2\sqrt{A_c/2} + 2K\sqrt{A_c/2}(A_c/2 - A^0).$$
$$(SM.14)$$

The cells will thus grow if

$$2K\sqrt{A_c/2}(A^0 - A_c/2) > \frac{\Lambda}{2}s + \Gamma s^2\sqrt{A_c/2}. \quad (SM.15)$$

Let us use the notation of Farhadifar et al. [2007], with the A^0 that they use to create the nondimensional parameters given by its mean value, $\langle A^0 \rangle$ during the cell

cycle in our model. The nondimensional parameters are $\bar{\Lambda} = \frac{\Lambda}{K\langle A^0\rangle^{3/2}}$ and $\bar{\Gamma} = \frac{\Gamma}{K\langle A^0\rangle}$. Let $A_c/(2\langle A^0\rangle) = c$ and the value of A^0 in Eq. SM.15 be $\beta\langle A^0\rangle$. Then cells will grow if

$$\bar{\Lambda}s/2 + \bar{\Gamma}s^2\sqrt{c} < 2\sqrt{c}(\beta - c). \qquad (SM.16)$$

If the model of target area variation with the cell cycle and the critical area for cell division are fixed, then, for a given shape index (e.g. that of a regular hexagon), this forms a diagonal region in the phase space.

We note that equations SM.13 and SM.15 imply that cells with lower shape indices (i.e. more regular and with larger number of sides) are more likely to be stable.

In Fig. S10, we show the phase diagram in the space of the parameters $\bar{\Lambda}$ and $\bar{\Gamma}$. Region I is where cells are expected to have negative interfacial tensions and so have irregular shapes since they do not want to minimise their perimeters. The boundary of this domain is at $\Lambda + \Gamma s\sqrt{A^0} = 0$, so $\bar{\Lambda} + \bar{\Gamma}s = 0$. We plot this for hexagonal cells ($s = 2 \times 3^{1/4}2^{1/2}$). In Region II, cells take regular shapes and the only stable size is positive. The other boundary of this domain is at $\Lambda = 0$ or $\bar{\Lambda} = 0$. In Region III, cells take regular shapes and small cells collapse, whilst larger ones grow to an equilibrium size. In Region IV, all cells collapse. The boundary between these regions is given by $A^0 = \frac{\Gamma s^2}{2K} + \frac{3}{4}\left(\frac{\Lambda s}{K}\right)^{2/3}$ or $2 = \bar{\Gamma}s^2 + \frac{3}{2}(s\bar{\Lambda})^{2/3}$. We plot this for hexagonal cells. We also show as the dotted line, a line below which all cells should grow (Eq. SM.16). Here $\beta = 0.68/1.25$ is the minimum value of A^0 divided by its mean value. The minimal value is calculated from Eq. (1), assuming mean growth rate, and $c = 1.3/(2 \cdot 1.25)$ is the critical area divided by twice the mean value of A^0 (all nondimensional units).

III. TISSUE ASPECT RATIO DEPENDS ON EXPANSION RATE, THE VALUE OF Γ AND ON HOW EFFICIENTLY CELLS REARRANGE

To gain insight into the anisotropic growth of the tissue, we consider a slightly simpler system. We assume all cells are identical with area A and we assume that $\Lambda/\Gamma << 1$, so that the target perimeter is negligible. We assume cell division is unorientated. Let the dimensions of the neural tube be $R(t)$ and $H(t)$ and the number of cells be $N_c(t)$. Therefore $N_cA = RH$. For ease of analysis, we assume that cells are rectangular. In the direction of R, there are n_1 cells of length l_1, with $R = n_1l_1$ and similarly in the other direction there are n_2 cells of length l_2. Therefore, $H/R = (n_2 l_2)/(n_1 l_1)$ and $N_c = n_1n_2$. We start with an equal number of square cells in each direction. We consider two extreme cases. In the first case, intercalation can take place rapidly, allowing the number of cells in each direction to change. In this case, any change in the tissue shape and the dissipation of drag

forces will occur predominantly by changing the number of cells in each direction, rather than by altering cell shape. In such a scenario, the shape of individual cells will be relatively unaffected by anisotropic forces and will be square, hence $n_2/n_1 = H/R$. In the second case, intercalation does not take place, in which case as the aspect ratio of the whole tissue changes, the cells change shape accordingly. In this case, the relative number of cells in each direction does not change, since cell division is unorientated and intercalation impossible, hence $n_1 = n_2$ and $l_2/l_1 = H/R$.

The expansion of the tissue in dimensions R and H and perimeter $L = 2(l_1 + l_2)$, is given by SM.3. On the shortest timescales, we assume only l_1 and l_2 change. Therefore

$$\partial E/\partial R = N_c K(A - A_0)\partial A/\partial R + N_c \Gamma L \partial L/\partial R$$
$$= HK(A - A_0) + 2N_c \Gamma L/n_1$$
$$= HK(RH/N_c - A_0) + 4n_2\Gamma(l_1 + l_2)$$
$$= H[K(RH/N_c - A_0) + 4\Gamma(1 + l_1/l_2)].$$
(SM.17)

Similarly,

$$\partial E/\partial H = R\left[K(RH/N_c - A_0) + 4\Gamma(1 + l_2/l_1)\right].$$
(SM.18)

In the first case, $\mu'/\mu'' \, dR/dH = H/R$ and the change in R^2 will be μ''/μ' times the change in H^2, so the aspect ratio, H/R, will tend to $\sqrt{\frac{\mu'}{\mu''}}$.

In the second case,

$$\mu' N_c \frac{dR}{dt} = H[K(A_0 - RH/N_c) - 4\Gamma(1 + R/H)]$$
$$\mu'' N_c \frac{dH}{dt} = R[K(A_0 - RH/N_c) - 4\Gamma(1 + H/R)].$$
(SM.19)

We expect that in the long term the growth will equilibrate so that the average areas and aspect ratios of cells will tend to constants, which we call $r = H/R$ and $A = RH/N_c$. Then we have that the length and height of the tissue satisfy

$$R = \sqrt{A/r}\sqrt{N_c}$$
$$H = \sqrt{rA}\sqrt{N_c}.$$

If we assume that cell numbers grow exponentially with rate λ, so that $\frac{dN_c}{dt} = \lambda N_c$, then substituting into Eqs. SM.19 gives

$$\frac{\lambda}{2}\sqrt{N_c}\mu'\sqrt{A/r} = \sqrt{rA}\sqrt{N_c}[K(A_0 - A) - 4\Gamma(1 + 1/r)]$$
$$\frac{\lambda}{2}\sqrt{N_c}\mu''\sqrt{rA} = \sqrt{A/r}\sqrt{N_c}[K(A_0 - A) - 4\Gamma(1 + r)].$$

Dividing by $\sqrt{N_c A}$ yields simultaneous equations for r and $A_0 - A$ with solution

$$r = \sqrt{\frac{\mu'\lambda + 8\Gamma}{\mu''\lambda + 8\Gamma}}$$

$$A_0 - A = \frac{8\Gamma + \sqrt{(\mu'\lambda + 8\Gamma)(\mu''\lambda + 8\Gamma)}}{2K}.$$

This means that when growth is slow so that $\mu'\lambda, \mu''\lambda << 8\Gamma$, as $t \to \infty$, the aspect ratio should tend to one. When growth is fast so that $\mu''\lambda, \mu'\lambda >> 8\Gamma$, the aspect ratio should tend to $\sqrt{\frac{\mu'}{\mu''}}$. As the exponential growth rate of the tissue varies from small to large, the asymptotic aspect ratio will vary monotonically between these two values. Slow tissue growth is defined by the regime in which perimeter forces greatly exceed drag forces and rapid tissue growth by the regime in which drag forces greatly exceed perimeter forces. Cell pressure due to area elasticity is always important. In slow growth, pressure generated by the difference between target area and mean area is balanced by the stretched actomyosin ring, whereas in rapid growth it is balanced by drag.

The most extreme aspect ratios are achieved when the actomyosin ring exerts a negligible force or when tissue rearrangement is extremely efficient.

Farhadifar, R., Röper, J.-C., Aigouy, B., Eaton, S. and Jülicher, F. (2007). The influence of cell mechanics, cell-cell interactions, and proliferation on epithelial packing. *Current Biology* **17**, 2095 – 2104. ISSN 0960-9822.

Magno, R., Grieneisen, V. A. and Marée, A. F. (2015). The biophysical nature of cells: potential cell behaviours revealed by analytical and computational studies of cell surface mechanics. *BMC Biophysics* **8**, 8. ISSN 2046-1682.
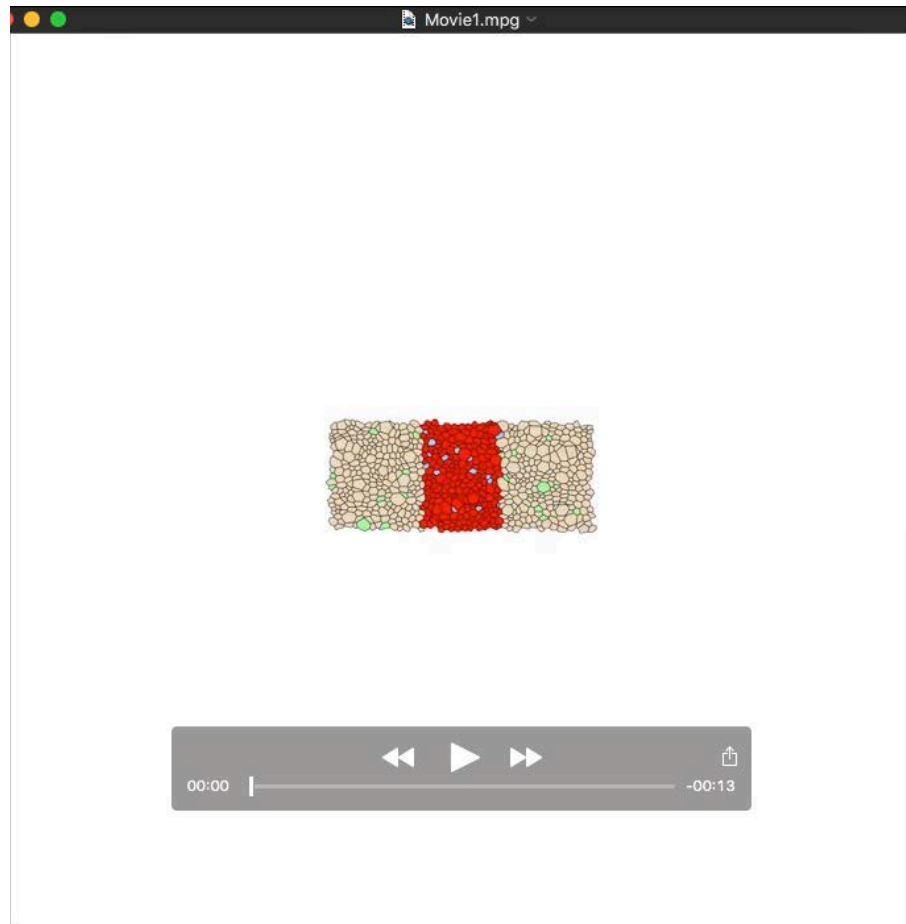
Movie 1. Simulation of clones tracked during the 48 h in a tissue with pD (brown) and pMN (red) populations. Green and blue cells represent clones in pD and pMN, respectively.